

pubs.acs.org/cm Article

Altering the Arrangement of Framework Al Atoms in MEL Zeolites Using Mixtures of Tetrabutylammonium and Sodium Structure-Directing Agents

Elizabeth E. Bickel, Alexander J. Hoffman, Songhyun Lee, Hannah E. Snider, Claire T. Nimlos, Natalie K. Zamiechowski, David D. Hibbitts, and Rajamani Gounder*



ABSTRACT: The arrangement of Al sites in zeolite frameworks influences the structure and speciation of Brønsted acidic hydroxyl groups and of metal cations and complexes that behave as active sites in acid and redox catalysis, but synthetic approaches to systematically alter Al arrangement have yet to be developed for many zeolite topologies. Herein, we report the synthesis of MEL zeolites with varied Al contents (Si/Al = 35-118) using tetrabutylammonium (TBA+; TBA+/Si = 0.3) as the organic structuredirecting agent (OSDA) and with fixed Al content (Si/Al ~ 50) using mixtures of inorganic (Na⁺) and organic (TBA⁺) SDAs of different charge density $[(Na^+/TBA^+)_{gel} = 0-5, (Na^++TBA^+)/Si = 0.3]$. MEL zeolites crystallized using TBA+ as the sole structuredirecting agent (SDA) contained one TBA+ per channel intersection [4 TBA+ per 96 T-site unit cell (u.c.)], with varying bulk compositions (Si/Al > 23) consistent with charge density mismatch theory. Aqueous-phase ion exchange conditions to use Co²⁺ as a selective titrant of proximal Al sites in MEL were determined and validated by a cation site balance on Co-MEL zeolites. MEL crystallized from TBA^+ alone contained finite fractions of Co^{2+} -titratable Al-Al pairs that increased $(2 \times Co^{2+}/Al = 0.2-0.4)$ with total Al content (Si/Al = 35-118), as also observed for MFI crystallized with tetrapropylammonium (TPA⁺) alone. MEL crystallized from mixtures of Na⁺ and TBA⁺ contained fractions of Co^{2+} -titratable Al–Al pairs that decreased (2 × Co^{2+} /Al = 0.22–0.10) with increasing occluded Na⁺ content (0.0–2.4 Na⁺/u.c.). Analysis of occluded OSDA and inorganic SDA content in MEL samples reveal evidence for competitive occlusion of Na⁺ and TBA⁺. Density functional theory-estimated energies reveal that Na⁺ co-occlusion with OSDAs is less likely in MEL than MFI frameworks. These findings, together with our prior results on MFI and CHA frameworks, indicate that site-isolated Al arrangements tend to form when monovalent inorganic SDAs and OSDAs compete for occupancy within void and ring spaces of zeolite frameworks.

...influences Al arrangement in Al-MEL

1. INTRODUCTION

Zeolites are crystalline, microporous materials composed of silicon tetrahedrally coordinated to oxygen. Substitution of Si⁴⁺ with a trivalent heteroatom (e.g., Al³⁺) results in an anionic charge on a lattice oxygen, which can be balanced by a proton (H⁺) that functions as a catalytic active site. The substitution of the framework Al among different crystallographically unique tetrahedral sites (T-sites) and in different relative proximity can lead to Brønsted acid sites of different strength¹ and reactivity.^{2,3} CHA zeolites possess a single crystallographically unique T-site, facilitating the development of quantitative probes of different Al–Al arrangements in CHA

and their connection to catalytic function. Density functional theory (DFT)-estimated Co²⁺ binding energies at different Al–Al ensembles in CHA indicated that Co²⁺ selectively titrates arrangements of two Al separated by one or two Si in

Received: April 9, 2022 Revised: June 30, 2022 Published: July 19, 2022





the CHA 6-membered ring (6-MR).^{4,5} Hoffman et al. reported methanol and ethanol dehydration first-order and zero-order rate constants (per H⁺) in CHA zeolites that were higher (up to 20×) at H⁺ sites associated with arrangements of two Al in a 6-MR, as quantified by Co²⁺ titration.^{3,6} Kester et al. reported first-order rate constants for monomolecular propane cracking (per H⁺, 748 K) that were higher (12 \times) at 6-MR paired Al sites than at 6-MR isolated sites in CHA.2 The number of possible Al-Al site pair arrangements increases drastically with decreasing symmetry of the zeolite topology; however, DFT estimates of Co²⁺ binding energies of different Al-Al site pairs can be used to identify likely binding sites for Co²⁺ in lower symmetry frameworks. DFT estimates of Co²⁺ binding energies for 202 of the 612 total possible Al-Al arrangements in a 96 T-atom MFI unit cell showed that arrangements of two Al in the 5- and 6-MRs of MFI zeolites are likely quantified by Co²⁺ titration. Higher fractions of Co²⁺-titratable Al–Al pairs in MFI have been correlated to higher rates of n-alkane cracking,^{7,8} propene oligomerization,^{9,10} and fructose dehydration.¹¹ Additionally, the proximity of Al in zeolite frameworks affects their behavior for adsorption processes, 12,13 as well as ion-exchange capacity and the speciation of metal cations and complexes used for various catalytic reactions, including partial methane oxidation, 14-17 methane dehydroaromatization, ¹⁸⁻²⁰ alkane dehydrogenation, ²¹⁻²³ and the reduction, decomposition, and storage of nitrogen oxides.^{24–31}

Despite growing recognition of the importance of Al arrangement in zeolites, 32-36 synthetic approaches to systematically vary Al proximity have yet to be developed for many zeolite topologies and oftentimes occur concomitantly with changes in other material properties such as the bulk Al content (Si/Al). Charge density mismatch (CDM) theory proposes that zeolite crystallization can occur at compositions wherein all framework Al sites can be balanced by the cationic structure-directing agents (SDAs) that occlude 37,38 within the rings and voids of the framework topology. Moreover, the specific arrangement and packing density of SDAs within zeolite rings and voids influence the preferred arrangements of Al atoms that become incorporated into the framework. Varying the ratios of two SDAs of different structures and charge density in synthesis gels (at fixed total SDA/Al and fixed synthesis time) has been shown to influence Al proximity (at fixed Si/Al) for several zeolite frameworks. 4,5,39-43 Di Iorio and Gounder reported that CHA synthesized (433 K, 6 days) with N,N,N-trimethyl-1-adamantylammonium cations (TMAda⁺) and Na⁺ contained fractions of 6-MR paired Al that increased (0.0-0.2) with increasing amounts of occluded Na⁺ (0.0-0.3 per cha cage).⁴² The total quantity of SDAs occluded within CHA materials increased with increasing Na⁺ $(\sim 1.0-1.4 \text{ per } cha \text{ cage})$ while the quantity of TMAda⁺ remained constant (~ 1 per cha cage), demonstrating that Na⁺ and TMAda⁺ co-occlude cooperatively in CHA.⁴ This experimental observation was rationalized by DFT energies computed for different arrangements of two Al in a 96 T-atom CHA unit cell (u.c.) charge-compensated by TMAda+ and Na+, which indicated that Na+ and TMAda+ show an energetic preference (10-30 kJ mol⁻¹) to co-occlude in configurations where Na+ is located in a 6-MR adjacent to the cha cage containing TMAda+ and where two Al are incorporated in a 6-MR. Nimlos et al. reported that the fraction of Co²⁺-titratable Al-Al pairs (i.e., 2 Al in 5- and 6-MRs) in MFI synthesized using combinations of tetrapropylammonium (TPA+) and Na+ as co-SDAs increased (0.02-0.34) with increasing Al content

(Si/Al = 37–185), and that the fraction of paired Al at fixed Al content (Si/Al = 50) generally increased (0.12–0.44) with the amount of Na $^+$ (1.1–2.4 per u.c.) occluded in the solid product. The amount of TPA $^+$ occluded in MFI samples remained approximately constant (\sim 3.2–4.0 per u.c.), while the total SDA content increased (to ca. 5.5 per u.c.) upon including Na $^+$ in synthesis gels, suggesting that Na $^+$ tends to cooperatively co-occlude with TPA $^+$ in MFI.

Not all combinations of monovalent SDAs with different charge densities are capable of co-occluding within a given zeolite in a cooperative manner because some co-occluded SDA configurations result in energetically unfavorable interactions of the SDAs with the framework and with each other. In contrast to CHA crystallized with Na⁺ and TMAda⁺, CHA crystallized with K⁺ and TMAda⁺ (433 K, 6 days) contained predominantly 6-MR isolated Al (2 × Co²⁺/Al < 0.1)4 and the amount of occluded TMAda+ systematically decreased as the amount of occluded K+ increased. The competitive occlusion of K+ and TMAda+ in CHA was rationalized by DFT-estimated energies for K⁺ and TMAda⁺ in a 96 T-atom CHA unit cell that showed K+ has an energetic preference to reside within 8-MR windows that causes TMAda+ occlusion in an adjacent cha cage to become energetically disfavored.⁴ DFT-computed energies also indicated that arrangements of two Al in the 8-MR of CHA were the most favorable arrangements of two Al charge-balanced by TMAda⁺ and K⁺, rationalizing the absence of Co²⁺-titratable 6-MR pairs in these CHA samples. Lv et al. reported that the fraction of 6-MR paired Al sites in CHA synthesized (423 K, 6 days) with combinations of TMAda+ and different alkali cations decreased with increasing size of the alkali cation (Li⁺ > $Na^+ > K^+ > Cs^+$), further suggesting that larger monovalent cations are unlikely to co-occlude with TMAda^{+,40} Thus, the siting preferences of monovalent organic SDAs (OSDAs) and inorganic SDAs within different rings and voids of the CHA structure influence their ability to occlude cooperatively or competitively, providing routes to form different Al arrangements.

The continued development of synthetic approaches to systematically vary framework Al arrangement, and characterization approaches to quantify this property, is needed for other zeolite topologies that may possess topological features that influence diffusion and reaction behavior for certain applications. MEL is composed of intersecting straight channels (5 Å in diam) that have been reported to facilitate diffusion, influence selectivity, and increase catalyst life-time in hydrocarbon upgrading reactions compared to MFI zeolites of similar composition and crystallite size. MEL can be synthesized with various SDAs⁴⁷ including N,N-diethyl-3,5-dimethyl piperidinium hydroxide, 48,49 1,8-diaminooctane (DAO), 50,51 and tetrabutylammonium (TBA+) 50,52-55 over a range of compositions (Si/Al = $19-\infty$). Wang et al. synthesized MEL (Si/Al = 40) in the presence of TBA+ and different alkali metal cations (Na+, Li+, and K+)52 and used Co^{2+} ion-exchange [0.05 M $Co(NO_3)_2$, 353 K, 12 h, 3×] to quantify the fraction of proximal Al sites, verifying the absence of Co-oxides with a site balance by quantifying residual H⁺ sites from IR spectra after pyridine titration. The fraction of Co²⁺-titratable Al-Al pairs was not influenced by the incorporation of Na^+ (Na^+/TBA^+ = 0.03) but decreased (0.41-0.24) upon addition of Li⁺ and Na⁺ to TBA⁺-containing synthesis gels ($Li^+/Na^+ = 0.07 - 0.50$, $Li^+/TBA^+ = 0.002 -$ 0.015). This decrease was attributed to Si/Al ratios (measured

by 29 Si MAS NMR) that systematically increased (Si/Al = 32–64) with increasing Li⁺/Na⁺, despite constant Si/Al in the gel (Si/Al = 40). Thus, while differences in Al arrangements have been observed in MEL crystallized with different SDA mixtures, a molecular description of the consequences of SDA siting and occlusion on Al proximity in MEL are not well understood.

Here, we report the synthesis of MEL zeolites with varied Al contents (Si/Al = 35-118) using TBA⁺ as an SDA and MEL zeolites with fixed Al content (Si/Al = 50) using mixtures of TBA+ and Na+ as co-SDAs. Methods to selectively titrate proximal Al sites in MEL using Co2+ were developed and validated and then used to quantify the number of proximal Al sites among MEL samples crystallized with different compositions (Si/Al) and from synthesis gels containing different amounts and ratios of TBA+ and Na+. MEL crystallized using TBA⁺ as the sole SDA possessed Al contents that were consistent with predictions from CDM theory and a finite number of Co²⁺ titratable Al-Al pairs that increased with increasing Al contents. The cooperative co-occlusion of TBA+ and Na+ should result in higher fractions of proximal Al sites (at fixed Si/Al) in MEL, which has a similar structure to MFI, yet Na⁺ and TBA⁺ were found to compete for occlusion within MEL voids. DFT calculations indicate that binding energies of Na⁺ are slightly weaker in MEL than in MFI with equal OSDA contents (per unit cell) in the composition range of MEL and MFI zeolites crystallized experimentally. The inclusion of Na⁺ in MEL synthesis gels led to a decrease in the fraction of Al pairs at fixed Al contents and H⁺ site density (Si/Al \sim 50, H⁺/ u.c. ~ 2) with increasing quantities of occluded Na⁺, indicating that the replacement of TBA+ with Na+ leads to the formation of isolated arrangements of Al. The findings herein enable systematic variation in Al proximity in MEL zeolites of the fixed composition, provide an experimental protocol for characterizing Al proximity in the MEL framework, and provide additional insights into the consequences of cooperative and competitive SDA occlusion within zeolites on the proximity of framework Al.

2. MATERIALS AND METHODS

2.1. Synthesis of MEL Zeolites. MEL zeolites were synthesized using mixtures of TBA+ and Na+ as co-SDAs. Synthesis gel molar ratios were 1 SiO₂/n Al(OH)₃/x NaOH/ 27 H₂O/ 0.32-x TBAOH. The ratio of Na⁺ to TBA⁺ [x/(0.32 - x)] varied between 0 and 5. For samples synthesized with TBA+ only, the Al content varied by adjusting the amount of Al added into the synthesis (at fixed TBA+/ Si). In a typical synthesis, 4.29 g of tetrabutylammonium hydroxide (TBAOH, 55%, Sachem) was combined with 10.42 g of tetraethyl orthosilicate (TEOS, 98%, Sigma-Aldrich) in a perfluoroalkoxy alkane jar and stirred until homogenized. In a separate jar, deionized water (18 M Ω , 21.01 g) was combined with 1.82 g of NaOH (97%, Sigma-Aldrich) and 0.07 g of aluminum hydroxide [Al(OH)₃, 99% SPI Pharma] and stirred until homogenized. This mixture was added to the TBAOH and TEOS mixture and stirred for 2 h. The total mass of the jar and synthesis gel was recorded. The solution was then stirred under ambient conditions with the lid partially removed for 12 h to allow ethanol to evaporate. The total mass of the synthesis gel and jar after stirring was measured, and deionized water was added until the mass of the synthesis gel and jar achieved the mass measured prior to evaporation (typically 10 g of water). The solution was then transferred to 45 mL Teflon-lined stainless-steel autoclaves (Parr Instruments) and placed in a forced convection oven (Yamato DKN-402C) at 443 K for 3 days.

After the zeolite crystallization was quenched, solids were washed $3 \times$ in deionized water, $3 \times$ in an acetone/water mixture [50% (w/w)],

and 1× deionized water (30 cm³ g_{sample}^{-1} per wash) or until the pH remained constant after successive washes. Solids were recovered via centrifugation and dried at 373 K in stagnant air and then treated in flowing air at 853 K for 10 h (6.9 × 10^{-5} mol s $^{-1}$, 0.0167 K s $^{-1}$ UHP, 99.999%, Indiana Oxygen) to remove the organic content.

2.2. Characterization of MEL Zeolites. The framework topology was verified using powder X-ray diffraction (XRD) after removal of the OSDA by high-temperature oxidative treatment. XRD patterns were collected on 0.01-0.03 g of MEL sample loaded into low dead-volume sample holders (Rigaku) at a scan rate of 0.0200 s^{-1} . A Rigaku SmartLab X-ray diffractometer with a Cu K α radiation (λ = 0.154 nm) source operating at 1.76 kW was used for these measurements.

Micropore volumes were calculated from N_2 adsorption—desorption isotherms (77 K) collected on H-form samples (0.03—0.06 g) pressed and sieved to a uniform size (180—250 μm) measured with a Micromeritics 3Flex Adsorption Analyzer. Samples were degassed by heating to 393 K under vacuum (0.167 K s $^{-1}$, <5 mmHg), holding isothermally for 2 h, heating to 623 K under vacuum (0.167 K s $^{-1}$), and holding isothermally for 9 h. Uptakes of liquid N_2 measured on degassed samples ($P/P_{\rm o}=0.05-0.35,~77$ K) were extrapolated to zero pressure and used to estimate micropore volumes. Micropore volumes measured by this method agreed ($\pm 5\%$) with micropore volumes estimated from a semilogarithmic derivative plot of the isotherm given by $\partial (V_{\rm ads})/\partial (\ln(P/P_{\rm o}))$ versus $\ln(P/P_{\rm o})$, in which the volume of N_2 adsorbed at the first minimum corresponds to the pressure at which micropores have been filled.

Thermogravimetric analysis (TGA, TA Instruments SDTQ600) with a thermogravimetric analyzer and differential scanning calorimeter was used to measure the OSDA content on zeolite solids recovered after synthesis. In a typical measurement, 0.01-0.02 g of the as-made sample was heated in flowing dry air $(6.9 \times 10^{-5} \text{ mol s}^{-1}, \text{UHP}, 99.999\%, \text{Indiana Oxygen})$ to 523 K (0.167 K s^{-1}) , held for 0.5 h to remove adsorbed water, and heated to 1073 K (0.167 K s^{-1}) to combust the occluded organic content. The weight loss during the second temperature ramp (523-1073 K) was taken to be the organic content. Uncertainties in the OSDA content estimated from TGA analysis were estimated by propagating the uncertainty in the mass of the sample loaded (ca. 5%).

Al, Co, Na, and Si contents were quantified by inductively coupled plasma optical emission spectroscopy (ICP-OES) on a ThermoFisher Scientific iCAP 7000 Series spectrometer. Samples were prepared by digesting 0.01–0.02 g of zeolite powder in 2.0–3.0 g of hydrofluoric acid solution (48 wt %) for 24 h followed by addition of 45–55 g of deionized water and approximately 1 g of nitric acid (40 wt %). [Caution: Appropriate personal protective equipment, ventilation, and other safety measures should be used when working with HF]. Elemental compositions were determined from calibration curves generated by elemental analysis measurements performed on standards of known concentration. Uncertainties in sample elemental compositions estimated from elemental analysis (e.g., Na⁺/u.c.) were estimated by propagating the uncertainties in sample mass and in the quantification of elemental compositions from the calibration curves.

Temperature-programmed desorption (TPD) of NH₃ used to quantify H⁺ sites on MEL samples and the residual number of H⁺ sites after ion exchange. Samples (0.02-0.06 g) were loaded into a quartz U-tube reactor and supported on either side by quartz wool plugs. TPD experiments were performed with a Micromeritics AutoChem II 2920 Chemisorption Analyzer. To quantify the number of H⁺ sites, NH₄-form MEL samples were held at 323 K for 0.5 h under flowing He (\sim 1.0 \times 10⁻⁵ mol s⁻¹, UHP, 99.999%, Indiana Oxygen) after which the temperature was increased to 873 K (0.167 K s⁻¹). To quantify the number of residual H+ sites after ion exchange, gas-phase NH3 titration of residual sites was performed prior to TPD by flowing NH₃ [500 ppm, balance He, Matheson, 1.4×10^{-5} mol (s g_{solid}^{-1})] over the sample at 433 K for 4 h and then flowing a wet He stream [\sim 3% H₂O, 1.4 × 10⁻⁵ mol (s g_{solid}⁻¹)] over the sample to desorb NH₃ bound at non-protic sites.⁵⁶ In both cases, desorption products were quantified with a residual gas analyzer (MKS Cirrus 3). Uncertainties for NH₃ TPD experiments were estimated by

Table 1. Physicochemical Properties of MEL Zeolites

sample ^a	$V_{\rm micro}^{b}/\rm cm^3~g^{-1}$	Si/Al (solid) ^c	Al/u.c.	H^+/Al^d	H ⁺ /u.c.	Co ²⁺ /Al ^f
$MEL(C)^e$	0.14	32	2.9	0.61	1.8	0.14
MEL(15,0.0)						
MEL(28,0.0)	0.16	35	2.7	0.64	1.7	0.20
MEL(98,0.0)	0.17	118	0.8	0.64	0.5	0.11
MEL(50,0.0)-1	0.17	61	1.5	0.48	0.7	0.12
MEL(50,0.0)-2	0.17	52	1.8	0.61	1.1	0.11
MEL(50, 0.1)	0.18	43	2.2	0.96	2.1	0.19
MEL(50,0.3)	0.17	58	1.6	1.06	1.7	0.19
MEL(50,0.5)	0.17	57	1.7	0.88	1.5	0.07
MEL(50,1.0)	0.14	50	1.9	0.98	1.9	0.06
MEL(50,1.5)	0.16	47	2.0	0.86	1.7	0.08
MEL(50,2.0)	0.16	55	1.7			
MEL(50, 2.5)	0.16	51	1.8	0.96	1.7	
MEL(50, 3.0)		44	2.1			
MEL(50,5.0)	0.09					

^aSample nomenclature is MEL(X,Y)-n. X = Si/Al ratio. $Y = Na^+/TBA^+$ in the synthesis gel. n indicates replicate syntheses. C indicates commercial sample (ACS Material). ^bCalculated from N_2 adsorption isotherms. Uncertainty is ± 0.01 cm³ g⁻¹. 'Determined by ICP-OES. Uncertainty is $\pm 10\%$. ^dDetermined by NH₃ TPD. Uncertainty is $\pm 10\%$. ^eCommercially obtained (ACS Material, MR-50). ^fDetermined by ICP-OES and NH₃ titration on Co-exchanged simples (see Section 3.2, Section S6, Supporting Information). Uncertainty is $\pm 10\%$.

propagating the uncertainties in the catalyst loading and in the quantification of NH_3 .

Scanning electron microscopy (SEM) images were collected on an FEI Quanta 3D FEG Dual-beam SEM instrument with an Everhart—Thornley detector for high vacuum imaging at voltages of 2–7 kV and a spot size range of 1–5 μ m.

2.3. Ion Exchange of MEL. Samples were prepared in the NH₄ form by aqueous-phase ion exchange with 1 M NH₄NO₃ solution $(100 \text{ cm}^3 \text{ g}_{\text{sample}}^{-1}, \text{ solid } \text{NH}_4 \text{NO}_3 \ge 98\%, \text{ Sigma-Aldrich}) \text{ while}$ stirring at ambient temperature for 24 h. H-form zeolites were prepared by heating dried NH₄-form zeolites in flowing air to 773 K for 4 h (6.9 \times 10^{-5} mol s^{-1} , 0.0167 K s^{-1} , 99.999% UHP, Indiana Oxygen). Na-form samples were prepared by aqueous ion exchange with 2.5 M NaCl (100 cm³ g_{sample}^{-1} , solid NaCl \geq 99.0%, Sigma-Aldrich) for 24 h at ambient temperature. Samples were washed with deionized water after Na or NH₄ exchange (30 cm 3 g_{sample} $^{-1}$, 4×) and dried overnight at 373 K. Co²⁺ titrations were performed on Na- and NH₄-form samples at different temperatures (ambient, 313, 333, and 353 K) by aqueous-phase ion exchange with Co(NO₃)₂ solutions [0.1-0.75 M, solid Co(NO₃)₂ 99 wt %, Sigma-Aldrich 150 cm³ g_{sample}^{-1}]. Afterward, samples were washed with deionized water (30 cm³ g_{sample}^{-1} , 4×), dried overnight at 373 K, and treated in flowing air $(773 \text{ K}, 4 \text{ h}, 0.0167 \text{ K s}^{-1}, 6.9 \times 10^{-5} \text{ mol s}^{-1}, 99.999\% \text{ UHP, Indiana})$ Oxygen).

2.4. Computational Methods. Fully periodic DFT calculations were completed using the Vienna Ab initio Simulation Package (VASP), $^{57-60}$ as implemented in the computational catalysis interface. Flanewaves were constructed using the projector augmented wave 62,63 method with an energy cutoff of 400 eV. The Perdew–Burke–Ernzerhof form of the generalized gradient approximation was used for all calculations with Grimme's DFT-D3 dispersion correction with Becke-Johnson damping. The Brillouin zone was sampled at the Γ -point for all calculations.

Optimizations were performed in two steps of increasing accuracy for greater efficiency. 61 In the first step, wave functions were converged when they varied $<10^{-4}$ eV, and structures converged when the forces on all atoms were <0.05 eV Å $^{-1}$, with forces computed using a fast Fourier transform (FFT) grid 1.5× the planewave cutoff. These criteria for electronic convergence can lead to inaccurate force calculations. Therefore, the same force cutoff was used in the second step (0.05 eV Å $^{-1}$) but with forces computed using wave functions converged to within $<10^{-6}$ eV and with an FFT grid 2× the planewave cutoff. Calculations with Na $^+$, TPA $^+$, and TBA $^+$ SDAs in the siliceous MEL and MFI frameworks were run with appropriate compensating background charge for the number of

cationic SDAs present. These periodic calculations with a dipole correction can introduce artifacts into calculated energies when the density of ions varies across unit cells of different sizes because of spurious Coulombic interactions across unit cell boundaries. 1,67 As such, these structures were also run as neutral radicals (e.g., Na $^{\bullet}$ and TBA $^{\bullet}$) with spin polarization. Some calculations include Na surrounded by an explicit H₂O solvation shell to compare the competition between bare or solvated Na with OSDAs. We examine the binding of Na(H₂O)_x species (x = 0, 2, and 4) up to 4 Na in the pores of MFI and MEL for structures with three and four OSDAs in the unit cell. We calculate the binding energies for the OSDA, $\Delta E_{\text{OSDA-Si,IBE}}$ as

$$\Delta E_{\text{OSDA-Si,BE}} = E[\text{OSDA-Z}] - E[\text{OSDA}] - E[\text{Z}]$$
(1)

where E[OSDA] is the energy of the gas-phase OSDA, E[Z] is the energy of the zeolite without that OSDA, and E[OSDA-Z] is the energy of the bound OSDA in the zeolite. The OSDA was run both as a neutral species with spin polarization and as a cation within and without the zeolite. Similarly, we can calculate the binding energy of the OSDA near a framework Al ($\Delta E_{\text{OSDA-Al,BE}}$), which yields a negative charge in the framework, as

$$\Delta E_{\text{OSDA-Al,BE}} = E[\text{OSDA}^{+} - \text{Z}^{-}] - E[\text{OSDA}^{+}] - E[\text{Z}^{-}]$$
 (2)

where $E[OSDA^+]$ is the energy of the gas-phase OSDA (only the cationic OSDA was used for these calculations), $E[Z^-]$ is the energy of the anionic zeolite with one Al absent in that OSDA, and $E[OSDA^+-Z^-]$ is the energy of the bound OSDA in the zeolite. Finally, we also calculate the binding of the $Na(H_2O)_x$ complexes

$$\Delta E_{\text{Na}(\text{H}_2\text{O})_x} = E[\text{Na}(\text{H}_2\text{O})_x - \text{Z}] - E[\text{Na}(\text{H}_2\text{O})_x] - E[\text{Z}]$$
(3)

where $E[Na(H_2O)_x]$ is the energy of the gas-phase $Na(H_2O)_x$ complex, $E[Na(H_2O)_x$ -Z] is the energy of the bound complex, and E[Z] is the energy of the zeolite without the adsorbing Na. These binding energies were calculated for both the cationic Na next to cationic OSDAs $(\Delta E_{Na(H_2O)_x})$ and for an uncharged radical Na next to uncharged OSDAs with spin polarization $(\Delta E_{Na(H_2O)_x})$ to determine how the inclusion of charge affects these binding energies. These binding energies for neutral Na $^{\bullet}$ and OSDA $^{\bullet}$ radicals were calculated because periodic DFT calculations with a compensating background charge can introduce additional artefacts into estimated binding energies depending on the charge density of the calculation. A parity plot of a subset of the Na $^{\bullet}(H_2O)_x$ and Na $^{+}(H_2O)_x$ binding energies

indicates that the trends for the two are similar (Figure S14, Supporting Information).

The orthorhombic MFI structure used in this work was created from the XRD data of van Koningsveld et al., ⁶⁷ with the *Pnma* space group and unit cell parameters of a=20.078 Å, b=19.894 Å, c=13.372 Å, and $\alpha=\beta=\gamma=90.0^\circ$. Prior work found that some MFI models can restructure when adsorbates are introduced to their pores but that this structure was suitably stable for such DFT calculations. ⁶⁸ The MEL framework was acquired from the database of the International Zeolite Association (IZA), ⁶⁹ with space group $I\overline{4}m2$ and unit cell parameters a=b=20.270 Å, c=13.459 Å, $\alpha=\beta=\gamma=90.0^\circ$. Four TBA+ molecules were added to each intersection in the siliceous MEL unit cell, and its unit cell parameters were optimized (ISIF = 3 in VASP), yielding the final unit cell parameters of a=20.3427 Å, b=20.2573 Å, c=13.5628 Å, $\alpha=89.2954^\circ$, $\beta=90.0927^\circ$, and $\gamma=90.0795^\circ$. These unit cell parameters were used for all subsequent calculations regardless of the SDA loading.

3. RESULTS AND DISCUSSION

3.1. Synthesis of MEL Zeolites with TBA+ Only. The physicochemical properties of Al-MEL samples synthesized in this work and of a commercial Al-MEL sample (ACS Material) are shown in Table 1. Samples are denoted MEL(X,Y), where X is the Si/Al ratio and Y is the Na^+/TBA^+ ratio in the synthesis gel. Duplicate syntheses were performed for some samples to assess reproducibility [denoted as MEL(X,Y)-1 or -2]. XRD patterns for samples synthesized with TBA⁺ alone at different Si/Al ratios (Figure S1, Supporting Information) showed peaks consistent with the MEL topology, with the exception of MEL(15,0.0) that remained amorphous after 3 days of hydrothermal treatment. Micropore volumes for samples synthesized with TBA⁺ alone (Si/Al_{solid} \geq 35) measured from N₂ adsorption isotherms (Figure S3, Supporting Information) were consistent with those measured on a commercially obtained MEL sample and values reported previously, 50,52,70 suggesting that these samples largely comprised crystalline MEL. The amount of occluded TBA+ was quantified by TGA on the as-made samples and is plotted in Figure 1. Approximately, four TBA+ were occluded per unit cell (96 T-site) for all MEL samples irrespective of the Al content (Figure 1), suggesting that one TBA+ occludes in each of the four channel intersections⁷¹ in the MEL unit cell, and that samples crystallized with fewer than 1 Al per intersection (Si/Al > 23) contain anionic lattice defects to charge-balance the remainder of the occluded TBA+. This finding is analogous to observations made for MFI synthesized with TPA+, wherein one TPA+ occludes per channel intersection. The lack of the crystalline product observed for MEL(15,0.0) is consistent with predictions from CDM theory, 37,38 which indicates that the maximum amount of Al that can be incorporated into a zeolite framework is limited by the amount of cationic SDA that can be occluded within the extra-framework void and ring spaces. The occlusion of four TBA+ per MEL unit cell (one per intersection) limits the amount of framework Al that can be incorporated to four per unit cell, corresponding to Si/Al = 23 (dashed line, Figure 1). Thus, MEL synthesis gels containing higher Al contents (Si/Al < 23) are unable to crystallize in the presence of TBA⁺ alone, analogous to MFI crystallized with TPA+ alone.

Next, we turn to DFT to evaluate the interaction between these OSDAs and the zeolite framework. DFT-calculated OSDA binding energies in siliceous zeolites ($\Delta E_{\rm OSDA-Si,BE}$) have been used to evaluate the suitability of OSDAs for the synthesis of specific frameworks and for the targeted synthesis

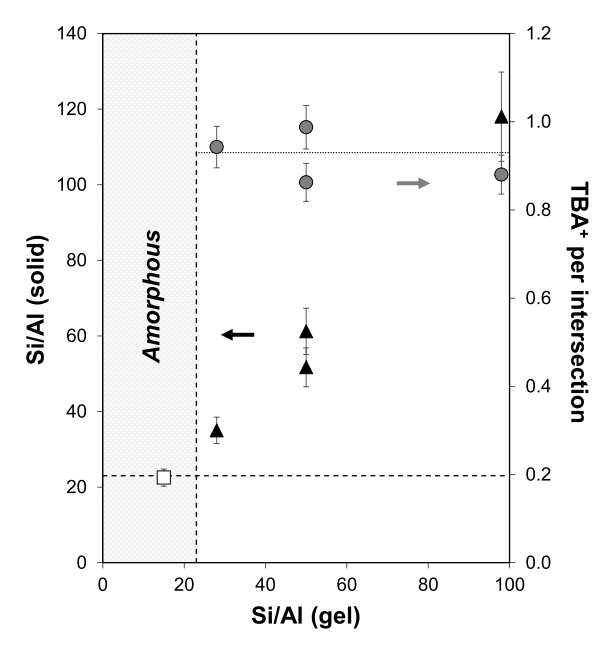
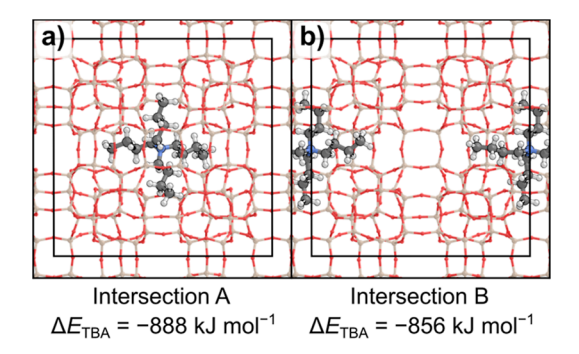


Figure 1. Si/Al of the solid crystalline product (\triangle) and amorphous product (\square), and TBA⁺ content occluded per intersection (gray \bullet) on MEL samples crystallized with only TBA⁺. Vertical and horizontal dashed lines indicate the predicted CDM limit (Si/Al = 23). The dotted line indicates the average TBA⁺ content occluded per channel intersection. Error bars reflect an absolute error.

of zeolite intergrowths.^{43,72} Here, we use these $\Delta E_{\text{OSDA-Si,BE}}$ to compare the topologies of MFI and MEL and the propensity of Na⁺ to displace OSDAs during zeolite synthesis for each framework.

MFI and MEL both have channel intersections; however, all intersections in MFI are equivalent while MEL possesses two unique intersections (Figure 2a,b). The intersections in MEL have different sizes: the A intersection is 30% larger than the B intersection.⁷³ As such, TBA⁺ binds more strongly in the A intersection ($\Delta E_{OSDA-Si,BE}$ of -888 kJ mol⁻¹) than in the B intersection (-856 kJ mol⁻¹). This finding is consistent with early computational studies⁷⁴ using force fields, which found that TBA+ binds more strongly in the A intersection by 59 kJ mol⁻¹. As OSDA loading increases, the next TBA⁺ binds to the other A intersection (-932 kJ mol⁻¹) and only then begins to fill the remaining two B intersections (-935 and -993 kJ mol⁻¹) (Figure 2c). While these binding energies become stronger (i.e., more negative) with each subsequent TBA+, this decrease is less pronounced once TBA+ begins to occupy B intersections, changing from -932 to -935 kJ mol⁻¹ between the second and third TBA+. In MFI, the sequential addition of TPA^+ results in ΔE_{OSDA} values linearly becoming more negative from -847 to -1012 kJ mol⁻¹. These results suggest that TPA+ binds more weakly in the intersections of MFI than TBA+ does in the A intersections of MEL but more strongly than TBA+ in the B intersections of MEL. The increase in binding strength with coverage observed for both zeolite-OSDA pairs is likely caused by van der Waals interactions between alkyl chains. It is unlikely to be caused by spurious charge interactions as those were found to be strongly dependent on unit cell volume, which are nearly identical for MFI and MEL (difference of $\sim 2\%$).

The strength of the interaction between the OSDA and a given Al location in the framework can be calculated using a binding energy of the OSDA near that Al ($\Delta E_{\text{OSDA-Al,BE}}$; eq 2).



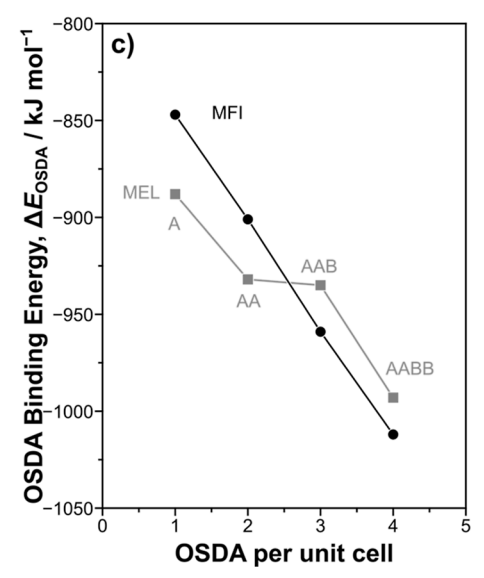


Figure 2. Structures and binding energies for TBA⁺ in (a) intersection A and (b) intersection B of MEL. (c) Differential binding energies of TPA⁺ in MFI and TBA⁺ in MEL for the most stable configuration of OSDA at each loading (1–4 OSDA per unit cell). The intersections containing TBA⁺ for the configuration at each loading are labeled in (c).

The preference for Al siting in a zeolite framework is partly governed by this $\Delta E_{\mathrm{OSDA-Al,BE}}$ value but also by the relative stability of the Al without the OSDA (ΔE_{Al} -), the stability of the OSDA in the given intersection, and additional kinetic factors that cannot be readily modeled. The combination of the first three of these values comprise the relative stability of the OSDA-Al configuration, $\Delta E_{\rm OSDA-Al}$. Our prior work analyzed both the $\Delta E_{\rm OSDA-Al}$, $\Delta E_{\rm OSDA-Al,BE}$, and $\Delta E_{\rm Al}^-$ in the MFI framework, which indicated that Al prefers to substitute in the T12 position. An identical analysis in MEL shows that Al is most stable at T1 absent in the charge-balancing OSDA $(\Delta E_{Al}^-, \text{Table 2})$. TBA⁺ binds most favorably near Al at the T2 and T4 locations in the A and B intersections, respectively. Critically, these two intersections do not contain the same Tsites: T1, T2, T6, and T7 are closest to the center of the A intersection, while the remaining T-sites are closer to the center of the B intersection. The combined effect of different TBA⁺ stabilities in each intersection, the differences in volumes of each intersection, and the proximity of certain T-sites to each intersection may lead to distinct Al distributions—and therefore catalytic behavior—in MEL samples with similar Si/ Al ratios but synthesized using different OSDAs.

We also modeled the interactions between the TBA⁺ and Al substituted farther from the N center of the OSDA. The interactions between the TBA⁺ and framework Al can be

Table 2. Relative Energies of Al Substitution at All T-Site Locations in MEL ($\Delta E_{\rm Al}^-$), the Distance between the N of the TBA⁺ and Al for the Most Stable Configuration of Al with TBA in Each Intersection ($r_{\rm N-Al}$), the Relative Stability of the TBA-Al Arrangement ($\Delta E_{\rm OSDA-Al}$), and the Lowest Binding Energy of the TBA⁺ Next to Each T-Site in Both Intersections ($\Delta E_{\rm OSDA-Al,BE}$)

		$r_{\text{N-Al}}/\text{Å}$		$\frac{\Delta E_{\mathrm{OSDA-Al}}}{\mathrm{kJ\ mol}^{-1}}$		$\Delta E_{ ext{OSDA-Al,BE}}/ ext{kJ-mol}^{-1}$	
T-site	$\Delta E_{\mathrm{Al}^-}/\mathrm{kJ} \ \mathrm{mol}^{-1}$	A	В	A	В	A	В
T1	0	6.23	8.71	0	35	-864	-830
T2	6	5.09	7.47	0	36	-871	-835
T3	3	7.60	5.75	11	26	-856	-841
T4	2	8.99	5.27	6	11	-860	-855
T5	4	8.00	6.06	12	21	-856	-848
T6	8	6.85	9.27	6	40	-867	-832
T7	14	5.73	8.09	8	42	-870	-837

described as a Coulombic interaction between the cationic N center of the TBA^+ and the anionic Al of the framework. By Coulomb's law, the relative energy of the TBA-Al arrangement should follow

$$\Delta E_{\text{OSDA-Al}} = \begin{cases} \frac{\alpha_{\text{A}} k_{\text{e}} q_{\text{OSDA}} q_{\text{Al}}}{r_{\text{N-Al}}} + \Delta E_{\text{Al}^-} + c_{\text{A}} \\ \text{in intersection A} \\ \frac{\alpha_{\text{B}} k_{\text{e}} q_{\text{OSDA}} q_{\text{Al}}}{r_{\text{N-Al}}} + \Delta E_{\text{Al}^-} + c_{\text{B}} \\ \text{in intersection B} \end{cases}$$
(4)

where q_{OSDA} and q_{Al} are the charges on each species (considered +1 and -1, respectively), r_{N-Al} is the distance between the N of the OSDA and the Al in the framework, k_e is Coulomb's constant (1389 Å kJ mol⁻¹ e⁻²), and α and c are parameters that can be tuned. There is only one unique intersection in MFI, so only one α and one c constant were needed to fit the data in our prior work; 5 in MEL, each intersection requires its own constant because of the changes in the stability of the TBA^+ (captured by the c values) and the relative permittivity (captured by the α values). When using a different constant for each intersection, we find good agreement between the energy predicted by this Coulombic model and the DFT-calculated values (MAE = 3.6 kJ mol^{-1} in MEL; Table 3 and Figure S13, Supporting Information). This fit for MEL is less precise than that for MFI, where the MAE was 2.0 kJ mol⁻¹ for a similar Coulombic prediction.⁵ This indicates that additional factors influence the DFT-calculated energies—for example, the longer chains of the TBA+ OSDA may introduce additional variability because they are more

Table 3. Parameters Used to Tune the Relative Permittivity (α) and the Stability of the OSDA (c) in Each Intersection of MEL for the Coulombic Interactions between the Cationic OSDA and Anionic Framework Al

location	lpha (unitless)	c/kJ mol ⁻¹
intersection A (MEL)	0.17	42.4
intersection B (MEL)	0.19	68.4
MFI^a	0.22	61.3

"Values for the MFI constants were published in a study by Nimlos et al. 5

strained when the cationic OSDA moves closer to the anionic Al or because their alkyl chains have more conformations than those of the TPA⁺ in MFI.

3.2. Synthesis of MEL Zeolites with Mixtures of TBA+ and Na⁺. The physicochemical properties of MEL samples synthesized with Na⁺ and TBA⁺ (Na⁺/TBA⁺ = 0-5) at Si/Al = 50 are summarized in Table 1. XRD patterns (Figure S2, Supporting Information) exhibited peaks characteristic of the MEL topology; however, with increasing Na⁺/TBA⁺ ratios in the synthesis gel, diffraction peaks characteristic of the MFI topology ($2\theta = 23.2$, 23.4, 24.5, and 45.5°) were also observed and became more pronounced with higher Na⁺ content. MFI impurities are often reported to form from TBA+ and TBA+/ Na⁺-containing gels and attributed to the similar structures of the two framework topologies and of TBA+ and TPA+ molecules. 52,75 SEM images were collected for MEL samples crystallized with different Na+/TBA+ ratios to determine whether this MFI impurity reflected crystallization of a separate MFI phase or the presence of MFI intergrowths within MEL crystallites. MEL samples crystallized in the absence of Na⁺ [MEL(50, 0.0)-2] consisted of small crystallites ($<0.1 \mu m \text{ diam}$) agglomerated to form sphere-like particles, while those synthesized in the presence of Na⁺ contained larger $(\sim 0.3-0.6 \ \mu m \ diam)$ crystallites (Figure S5, Supporting Information). MEL samples crystallized from Na+-dilute gels (Na⁺/TBA⁺ ≤ 1.5) consisted of crystallites of uniform morphology, yet those crystallized from Na+-rich gels (Na+/ $TBA^+ \ge 2.0$) also contained larger crystals with a coffin-shaped morphology, as is often characteristic of MFI crystallites (Figure S5, Supporting Information). These observations suggest that the MFI impurity in samples crystallized from more Na+-rich synthesis gels likely reflects the formation of a distinct MFI phase present as coffin-shaped crystallites. The presence of MFI phase impurities for samples crystallized with synthesis gels containing higher Na⁺ content is consistent with the ability of Na⁺ to act as a SDA for MFI crystallization (i.e., OSDA-free synthesis). MFI impurities may also occur within MEL samples crystallized with Na⁺/TBA⁺ \leq 1.5, as suggested by a small XRD peak characteristic of MFI at 45.5°; however, the low intensity of these peaks and appearance of crystallites of uniform morphology in SEM images of these samples suggest that these impurities are intergrowths and are not present in significant quantity. Thus, we focus the remainder of our study on samples crystallized from Na+-dilute gels (Na+/ $TBA^+ \leq 1.5$), for which XRD patterns and N₂ adsorption isotherms indicate that samples are predominantly the MEL topology, and SEM indicates that monodisperse crystallites were formed.

The amounts of Al, and occluded Na⁺ and TBA⁺, in MEL samples synthesized with different Na⁺/TBA⁺ ratios are shown in Figure 3. MEL samples synthesized with TBA⁺ alone contained a total of four SDA cations occluded per unit cell, while MEL samples synthesized with TBA⁺ and Na⁺ contained larger amounts of occluded SDA cations. Synthesis gels of low Na⁺ content (Na⁺/TBA⁺ = 0–0.5) crystallized MEL samples that systematically occluded a larger amount of SDA cations (from 4 to 5 per u.c.) with increasing Na⁺ gel content, and synthesis gels of higher Na⁺ content (Na⁺/TBA⁺ = 0.5–1.5) crystallized MEL samples with five total SDA cations occluded per unit cell (Figure 3). All MEL samples contained \sim 2 Al per unit cell, indicating that some occluded SDA cations were charge-balanced by anionic lattice defects rather than framework Al. With increasing Na⁺ content in the gel, the occluded

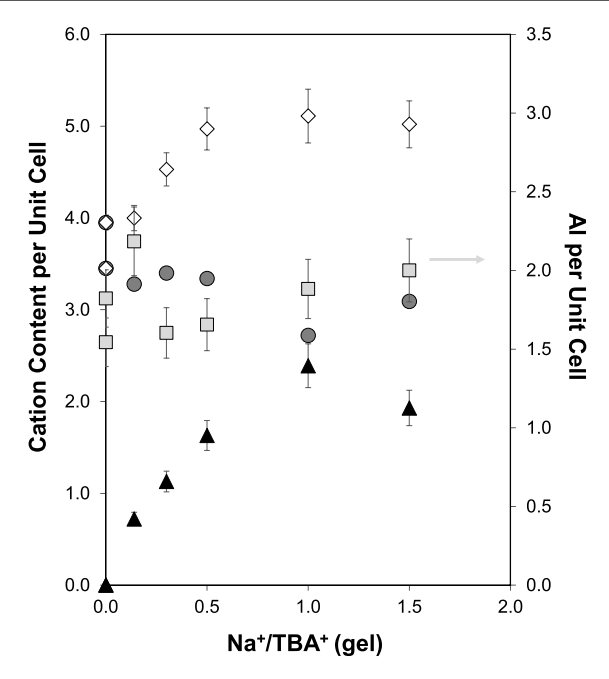


Figure 3. Total SDA ($TBA^+ + Na^+$) content (\diamondsuit), TBA^+ content (gray \bullet), and Na^+ content (\blacktriangle) occluded per unit cell shown on the left ordinate axis, and Al per unit cell (gray \blacksquare) shown on the right ordinate axis, for Al-MEL synthesized with different Na^+/TBA^+ ratios. Error bars reflect an absolute error.

TBA⁺ content decreased from an average of 3.7 to 2.7 per unit cell, while the occluded Na⁺ content increased from 0.7 to 2.4 per unit cell (Figure 3). Thus, the addition of Na⁺ to TBA⁺-containing synthesis gels generally led to a decrease in the occluded OSDA content but an increase in the total occluded SDA content, similar to previous observations reported for TPA⁺ and Na⁺-containing synthesis gels used to synthesize MFI zeolites.⁵

The increase in the occluded SDA content to 5 per unit cell upon the inclusion of Na⁺ in the synthesis gel suggests that Na⁺ influences the crystallization of MEL samples to form a compositional phase distinct from that in samples crystallized with TBA⁺ alone. The occlusion of 5 TBA⁺ molecules per unit cell is not possible with TBA+ alone because it is restricted to reside within channel intersections (4 per unit cell); thus, the use of Na⁺ and TBA⁺ as co-SDAs provides a route to crystallize MEL materials with a larger equivalent of occluded SDA cations per unit cell. The distinct compositional phase of MEL samples crystallized with and without Na⁺ is further evidenced by distinctions in the properties of these samples. The number of H⁺ sites was similar to the amount of Al for samples synthesized with Na⁺ and TBA⁺ (H⁺/Al = 0.86-1.06, Table 1), suggesting that these samples contain predominantly framework Al. In contrast, the number of H⁺ sites measured on samples synthesized with TBA+ alone was much lower than the amount of Al in these samples $(H^+/Al = 0.48-0.61)$. These data are consistent with ²⁷Al MAS NMR spectra, which showed a peak around 0 ppm for octahedrally coordinated Al^{77,78} on MEL samples crystallized with TBA⁺ alone (Figure S8, Supporting Information), while this feature was notably absent for samples crystallized with Na⁺ and TBA⁺ (Figure S9, Supporting Information). Additionally, SEM images of MEL synthesized with and without Na+ (Figure S5, Supporting Information) reveal morphological differences between these samples. Samples containing both Na⁺ and TBA⁺ possessed

larger crystallite sizes (\sim 0.3-0.6 μ m diam), while those crystallized with TBA+ only were composed of smaller, aggregated crystallites (\sim 0.1 μ m diam). Inclusion of inorganic cations in zeolite synthesis gels has previously been proposed to influence the dominant zeolite crystallization mechanism.⁷ Inclusion of Na⁺ in silicalite-1 synthesis gels was reported to promote crystal growth via a non-classical crystallization pathway (e.g., coagulation of nanoparticles) rather than classical pathways (e.g., layer-by-layer growth) because Na+ screens the electrostatic repulsion between the surfaces of nanoparticles caused by negatively charged surface oxygen atoms during crystallization, thereby facilitating coagulation of these nanoparticles.⁷⁹ Taken together, these observations suggest that the inclusion of Na⁺ in MEL synthesis gels results in the crystallization of MEL samples with distinct properties compared to those crystallized with TBA+ alone, possibly reflecting different crystallization pathways promoted by the presence of Na⁺.

The decrease in occluded TBA⁺ content among MEL samples crystallized from Na⁺-containing synthesis gels is more clearly illustrated by plotting the occluded TBA⁺ content against the occluded Na⁺ content (Figure 4). A linear

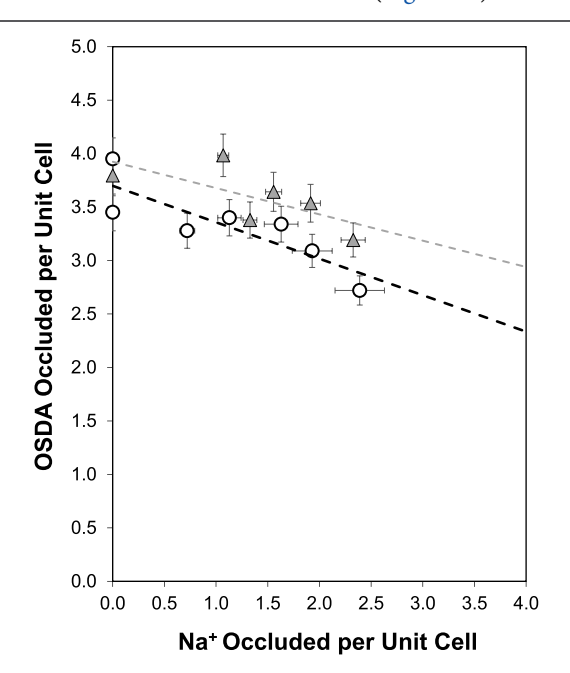


Figure 4. TBA $^+$ content occluded on MEL samples (O) and TPA $^+$ contents occluded in MFI crystallized with mixtures of TPA $^+$ and Na $^+$ (published in Nimlos et al. Distribution plotted against occluded Na $^+$ content (gray \blacktriangle). Dashed lines represent linear regressions to the data. Error bars reflect an absolute error.

regression of these data among all samples extrapolates to the limit of TBA⁺ occluded in an Na⁺-free synthesis (\sim 3.7 TBA⁺ per unit cell); however, this fit underpredicts the occluded TBA⁺ content for the two samples crystallized from gels with lower Na⁺/TBA⁺ ratios (0.3–0.5) and overpredicts the occluded TBA⁺ content for the sample crystallized from the gel of the highest Na⁺/TBA⁺ ratio (1.0). Thus, we conclude that Na⁺ occludes in MEL samples of two distinct compositional phases as the Na⁺/TBA⁺ ratio in the synthesis gel varies. At low Na⁺/TBA⁺ ratios, some Na⁺ is able to coocclude with TBA⁺, leading to an increase in the total occluded SDA content from 4 to 5 per unit cell without significant

displacement of TBA⁺ (Figure 3); however, higher Na⁺/TBA⁺ ratios lead to further Na+ incorporation and displacement of TBA+ from MEL channel intersections (Figure 4). The occluded TPA+ content previously reported5 for MFI samples crystallized with mixtures of TPA+ and Na+ and is also shown plotted against occluded Na+ content in Figure 4. A linear regression fit to these data extrapolates to a limit of ~4 TPA+ per unit cell, analogous the limit of ~4 TBA+ per unit cell occluded in MEL; however, the slope of this regression is slightly lower for MFI (ca. -0.25) than that for MEL (ca. -0.34), indicating that co-occlusion of Na⁺ and the OSDA is less favorable in MEL than MFI. These results indicate that repulsion between Na+ and TBA+ along with other steric hindrances in MEL limits the total SDA loading more than in MFI, possibly because of a stricter spatial limitation on Na⁺ incorporation into MEL and because TPA+ occlusion is slightly more favorable in MFI compared to Na⁺ and TBA⁺ in MFI.

In contrast to MFI, the MEL unit cell contains channel intersections of different diameters: two that are similar in size to the channel intersection of MFI (~0.7 nm; the B intersection in this work) and two that are slightly larger in volume (by $\sim 30\%$; the A intersection in this work). 45,71,73,74 Molecular mechanics simulations have suggested that occlusion of TBA+ in the larger channel intersections is more energetically favorable (by ca. 51-59 kJ mol⁻¹) than that in the smaller channel intersections. 71,74 Similarly, our findings here show that TBA+ prefers to occlude in the larger A intersection. Steric hindrances for TBA+ occluded in MEL may arise because of the larger alkyl chains of the OSDA or because of the volumetric and geometric differences between the accessible pores of MEL and MFI. We next calculate the energies to incorporate Na+ with the OSDAs for both MFI and MEL to determine whether these energies indicate coocclusion is more favorable for MFI than MEL, as suggested by the synthesis results. While calculations of the OSDAs and inorganic SDAs in CHA were completed with the chargecompensating framework AlO₄-, MEL and MFI have much lower symmetry—with 7 and 12 crystallographically unique Tsites—than CHA, rendering a rigorous investigation of Al siting with these SDAs intractable. Thus, we examine only the ability of these Na⁺ SDAs to co-occlude alongside OSDAs in the siliceous form of these frameworks; however, we include H₂O solvation shells of 2, 4, and 6 H₂O per Na⁺ to mimic more closely the hydrothermal synthesis conditions. We primarily focus on those with solvation shells of 2 and 4 H₂O because Na⁺ with 6 H₂O only fits in the zeolite when one OSDA has been removed (Figure S19, Supporting Information). While these calculations exclude anionic Al in the zeolite framework, the compensatory background charge included in these DFT calculations should permit us to study the interactions between cationic inorganic SDAs and OSDAs. Moreover, previous studies have used binding energies of OSDAs in siliceous zeolites to determine their fitness for templating a given framework, 43,72,80-85 indicating that the interactions among SDAs and between SDAs and zeolite hosts can be elucidated absent framework anions. Including Al may alter the preferred location of the Na⁺ or the OSDAs (e.g., by pulling them closer to the surrounding framework), but we do not expect it to significantly change our predictions of how readily these ions co-occlude within the intersections of these zeolites. Na⁺ cations are likely too large to sit within the small rings of MEL or MFI and, as such, closer siting to the zeolite

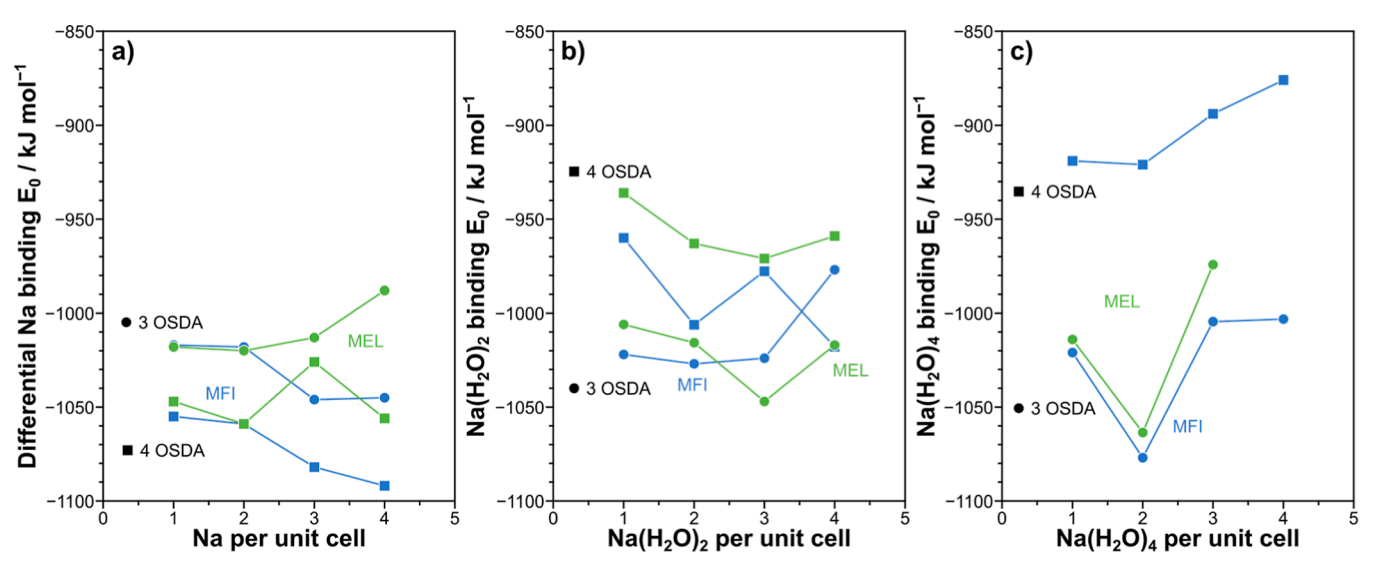


Figure 5. Na cation (Na⁺) binding energies (a) without H_2O , (b) with two H_2O per Na, and (c) with four H_2O per Na with three OSDA (\blacksquare) and four OSDA (\blacksquare) per unit cell in MFI (blue) and MEL (green). TPA⁺ was the OSDA in MFI and TBA⁺ in MEL.

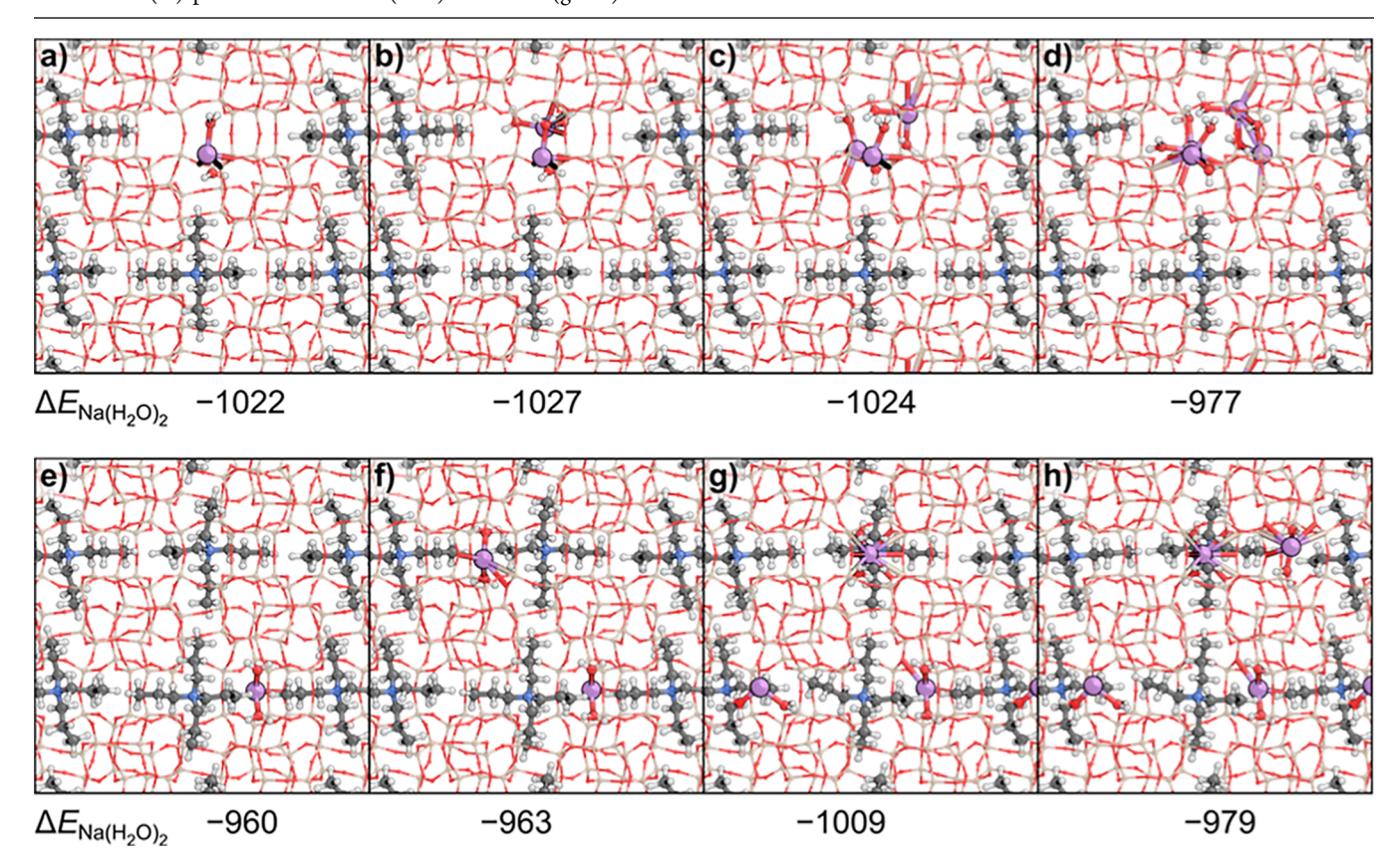


Figure 6. MFI structures with (a-d) three TPA⁺ and (e-h) four TPA⁺ and (a,e) one, (b,f) two, (c,g) three, or (d,h) four Na⁺ $(H_2O)_2$ occluded with the TPA⁺.

framework when Al is included is unlikely to change our conclusions.

DFT-calculated Na⁺ binding energies in MFI and MEL indicate that bare Na⁺ binds more strongly with four OSDA than with three OSDA (Figure 5a). Na⁺ by itself under vacuum is unstable, and the solvation provided by the additional OSDA strengthens its calculated binding energy. The first Na⁺ binds with similar strength in both MFI and MEL for both OSDA loadings, indicating that a bare Na⁺ cation may co-occlude at low loadings with these OSDAs in either framework. In MFI,

Na⁺ binding energies become more exothermic by 30–40 kJ mol⁻¹ (*i.e.*, bind more strongly) as Na⁺ loading increases from 1 to 4 Na⁺ ions per u.c., regardless of whether there are three or four OSDAs present in the framework. This suggests that the limit of six SDA observed in synthesized MFI at varying Na⁺/TPA⁺ gel ratios⁵ is not caused by steric repulsions between Na⁺ and TPA⁺ if Na⁺ incorporates as bare cations. Instead, the SDA loading is likely limited by the formation of high densities of anionic Al and defect sites in the MFI framework. In contrast to MFI, Na⁺ binding energies in MEL

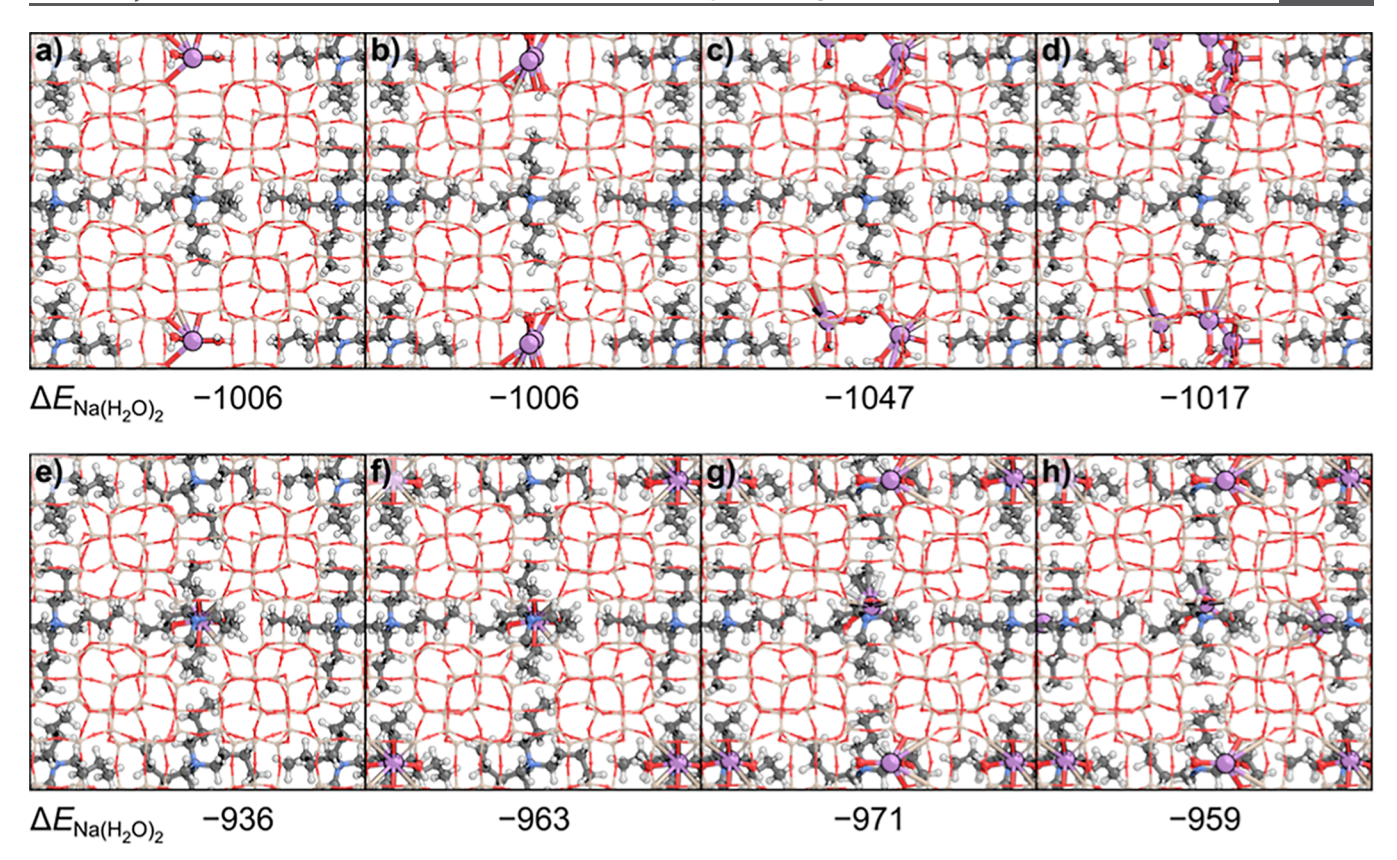


Figure 7. MEL structures with (a-d) three TBA⁺ and (e-h) four TBA⁺ and (a,e) one, (b,f) two, (c,g) three, or (d,h) four Na⁺ $(H_2O)_2$ occluded with the TBA⁺.

become less exothermic with increasing Na^+ loading, suggesting that there may by some additional repulsion between the Na^+ and TBA^+ , and that Na^+ – TPA^+ mixtures may be more likely to co-occlude in MFI than Na^+ – TBA^+ in MEL. However, zeolites are synthesized using hydrothermal methods and, therefore, Na^+ may be partially solvated by H_2O in the zeolite pores, which we evaluate next.

Including two H₂O molecules per Na⁺ changes the preferences for binding: Na⁺(H₂O)₂ binds more favorably with three OSDAs in the unit cell of each zeolite instead of four OSDAs (Figure 5b). This shift indicates that the H₂O stabilizes the gas-phase Na+ more than the bound cation and suggests steric hindrance and competition between Na⁺(H₂O)₂ and TPA+ or TBA+ in MFI or MEL, respectively. However, differential binding energies for Na⁺(H₂O)₂ are weakly dependent on Na loading in both MFI and MEL regardless of the OSDA loading. Similar to our findings for bare Na+, the weak dependence of Na+ binding energies on Na+ loading indicates that the total SDA content is not limited by the repulsion between the OSDA and inorganic SDA species. There is space in the zeolite for high loadings of both the OSDA and hydrated Na+; instead, this suggests that the density of anionic Al sites and siliceous defects in the framework limit total SDA incorporation during synthesis. Additionally, binding energies for Na+(H2O)2 in MFI are generally more negative (stronger) than those in MEL regardless of OSDA loading, indicating that under hydrothermal synthesis conditions, Na+ with a hydration shell is more likely to co-occlude with OSDAs in MFI than MEL.

The difference in binding energies between MEL and MFI is caused by changes in the binding sites of $Na^+(H_2O)_2$ in the

two frameworks. When only three TPA^+ are present in the MFI unit cell, all $Na^+(H_2O)_2$ occupy the same intersection (Figure 6a–d). This concentration of hydrated Na^+ in a single intersection provides further evidence that H_2O effectively solvates Na^+ ions better than the surrounding zeolite. Despite the high concentration of cationic charge, Na^+ can remain close to one another—and indeed prefer to remain close—because of the surrounding H_2O . When all intersections are occupied by TPA^+ , however, $Na^+(H_2O)_2$ prefer to distribute themselves among the channels equally in the small interstices between the propyl chains of TPA^+ (Figure 6e–h). Notably, Na^+ remain near the walls of the zeolite pore at each of these loadings. Despite the hydrophobicity of siliceous zeolites, their O atoms retain enough negative charge to interact with the cationic Na^+ despite the stability conferred by the hydration

Similar to MFI, when only three TBA⁺ are present, hydrated Na⁺ cations prefer to occupy the vacant intersection up to four Na⁺(H₂O)₂, where H₂O again permits Na⁺ to stay near one another despite the high cation concentration (Figure 7a–d). Because TBA⁺ binds more weakly in the B intersection, Na⁺ is more likely to displace TBA⁺ in this position. Indeed, the most stable structure at each Na⁺(H₂O)₂ loading with three TBA⁺ contained a B intersection without TBA⁺ and was 23 kJ mol⁻¹ more stable on average than the best structure with TBA⁺ removed from the A intersection. When four TBA⁺ are present, Na⁺(H₂O)₂ first occludes in the A intersections and then fills the B intersections (Figure 7e–h). The binding energies for the hydrated Na⁺ are generally higher than those in the MFI structure with four TPA⁺ per unit cell. These data indicate that hydrated Na⁺ co-occlude less favorably with the OSDA in

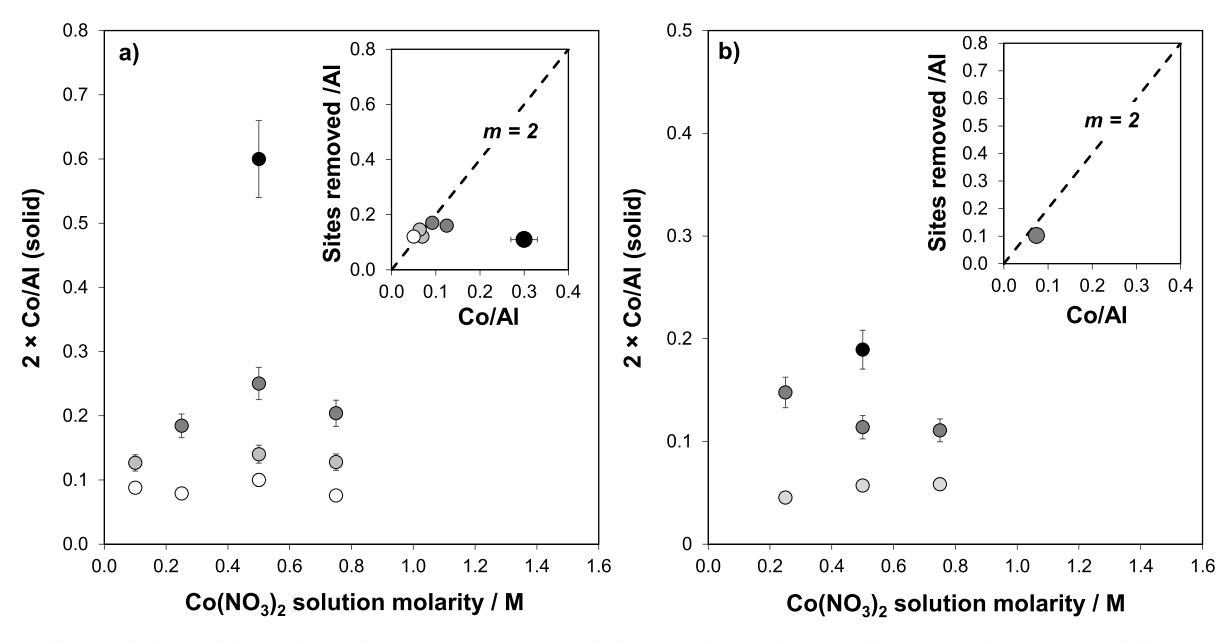


Figure 8. (a) MEL(C) and (b) MEL(50,0.5) exchanged at ambient (O), 313 K (gray \bullet), 333 K (dark gray \bullet), and 353 K (\bullet), on NH₄-form MEL. The insets show the site balances of divalent Co²⁺ and residual H⁺ cations after Co titration [0.25–0.75 M Co(NO₃)₂]. The dashed line corresponds to the removal of two monovalent cations with each divalent Co²⁺ ion. Error bars reflect an absolute error.

MEL than in MFI. Furthermore, $Na^+(H_2O)_2$ is more likely to displace TBA^+ specifically in the B intersection and occupy the now-vacant space because the B intersection is smaller, and TBA^+ does not remain in the B intersection as readily as the A intersection.

Additionally, we calculated binding energies for Na⁺ surrounded by four water molecules. As observed for Na⁺(H₂O)₂, the binding energies for Na⁺(H₂O)₄ are more negative at all Na loadings in MFI than in MEL when three OSDAs are present (Figure 5c). Furthermore, no Na⁺(H₂O)₄ species can be included in the MEL framework while retaining their water solvation shells with four TBA⁺ present. In MFI, however, the smaller alkyl chains on the TPA⁺ species leave more room to allow for Na⁺(H₂O)₄ species in the channels (structures shown in Figures S17 and S18, Supporting Information), although their binding energies are \sim 40 kJ mol⁻¹ less negative than those for the equivalent loadings of Na⁺(H₂O)₂.

These DFT data of $Na^+(H_2O)_x$ binding energies suggest that solvated complexes bind less strongly with increasing solvation size (x = 0, 2, or 4), more strongly in MFI than in MEL, and do not significantly weaken with Na^+ content. Qualitatively, this suggests that Na^+ species are more likely to co-occlude with OSDAs in MFI than in MEL, consistent with the experimental observations of a greater decrease in the OSDA content with increasing Na^+ content in MEL compared to MFI (Figure 4) and with the formation of the MFI phase impurities in samples crystallized in more Na^+ -rich synthesis gels (Figures S2 and S5, Supporting Information).

3.3. Validation of Co²⁺ Exchange Methods to Quantify Proximal Al Sites in MEL Zeolites. A major challenge in designing zeolite materials with varied Al proximity lies in the dearth of characterization methods available to precisely define and quantify this property. Among different approaches currently available to characterize Al proximity (e.g., IR OH spectroscopy and M²⁺ cation titration),^{2,42,86,87} the titration of Al–Al ensembles with Co²⁺ has emerged as a ubiquitous probe of Al proximity because of

the ability of Co²⁺ to selectively titrate specific subsets of Al—Al arrangements and because experimental ion-exchange conditions that selectively populate divalent Co²⁺ rather than other Co species (e.g., Co-oxides) are readily identifiable. Additionally, subsets of proximal Al likely to serve as the preferred binding sites for Co²⁺ have been identified with DFT for CHA (two Al in a 6-MR) and MFI (two Al in a 4-, 5-, or 6-MR).^{4,5} Thus, we will use Co²⁺ uptake as a quantitative metric of differences in Al proximity among different H-MEL samples and refer to subsets of proximal Al that are Co²⁺ titratable as Al—Al pairs (or "paired Al").

The use of Co²⁺ titration to quantify Al-Al pairs requires that ion-exchange conditions be chosen such that all Co²⁺titratable Al-Al pairs on a given zeolite sample are titrated without the concurrent formation of other species (e.g., Cooxides or hydroxides). The predominant presence of Co²⁺ on zeolite materials can be confirmed by quantifying residual H+ sites to verify an exchange stoichiometry of 1 Co²⁺ per 2 H⁺ sites, and the absence of Co-oxides can be further verified using UV-visible spectroscopy. Experimental protocols to quantitatively probe Al proximity using Co²⁺ titration have been developed successfully for the CHA and MFI frameworks; 5,42 however, ion-exchange conditions leading to saturation of Co-titratable Al-Al pairs without the concurrent formation of Co-oxides may vary across different topologies. Thus, current best practices suggest that Co²⁺ titration conditions must be identified for each framework. 5,42

A commercially available Al-MEL sample [MEL(C)] and representative MEL samples crystallized with and without Na⁺ [MEL(50,0.0)-2 and MEL(50,0.5)] in this study were used to identify conditions for selective Co^{2+} titration of Al–Al pairs in MEL. These MEL samples in the NH₄ form were exchanged with $\text{Co}(\text{NO}_3)_2$ solutions of different molarity (0.10-0.75 M) and at different temperatures (298-353 K) for 24 h. The amount of Co^{2+} retained on MEL(C) and MEL(50,0.5) for each exchange condition is shown in Figure 8. For both samples, the amounts of retained Co^{2+} did not change significantly with increasing $\text{Co}(\text{NO}_3)_2$ concentration for any

temperature, suggesting that saturation of Co²⁺-titratable Al-Al ensembles at these temperatures is achieved at low Co²⁺ molarities (≤ 0.10 M); however, amounts of retained Co²⁺ did increase with the increasing temperature [e.g., Co/Al = 0.05-0.22 for MEL(C)]. A cation site balance was used to assess whether the increase in Co/Al with increasing temperature reflected titration of additional Al-Al pair sites with Co²⁺ or the formation of other species (e.g., Co-oxides). If Co-oxides are not formed, two H⁺ sites should be removed per Co²⁺ on the Co-form MEL samples, and this can be estimated by quantifying residual H+ sites by NH3 titration (dashed line, inset, Figure 8); such a behavior is observed for Co²⁺ titrations performed at temperatures at or below 333 K with the exception of one outlier (additional discussion in Section S6, Supporting Information). In contrast, the number of H⁺ sites that would need to be exchanged if all Co species were present as ion-exchanged Co^{2+} (2×Co/Al $_{\text{solid}})$ was significantly higher than the number of H+ sites that were actually removed as quantified by NH3 titration on Co-MEL samples prepared from ion-exchange performed at 353 K, indicating that these temperatures result in the formation of Co-oxides. Importantly, the same number of H⁺ sites were removed by Co²⁺ titration at 353 and 333 K, suggesting that all Co-titratable Al-Al site pairs are saturated at 333 K, and that the predominant effect of higher temperature (353 K) is to promote the formation of non-ion-exchanged Co species. The saturation of Co²⁺-binding sites on the NH₄ form of MEL at 333 K was further corroborated by similar Co uptakes measured on the Na form of MEL(C) (Figure S10, Supporting Information) when ion exchange was performed at equivalent conditions. Thus, we conclude that Co2+ titratable Al-Al arrangements in MEL samples can be fully titrated at 333 K using Co(NO₃)₂ solutions (0.25-0.75 M). These Co²⁺ titratable subsets of Al—Al ensembles will hereafter be referred to as proximal Al. Notably, the formation of non-ion-exchanged Co species (e.g., Co-oxides) was observed for MEL samples synthesized with TBA+ only. The protocol used to quantify proximal Al for MEL samples crystallized with TBA+ only is discussed further in Section S6 (Supporting Information).

3.4. Influence of Al and SDA Contents on the Al **Arrangement in MEL Zeolites.** The fraction of proximal Al sites in MEL with varied Si/Al (35-118) synthesized with TBA⁺ alone is shown in Figure 9 and reported in Table 1. MEL samples crystallized with TBA+ alone contained fractions of paired Al that increased monotonically with increasing Al contents (Figure 9). This monotonic increase in paired Al with increasing bulk Al content demonstrates that these properties are correlated in MEL crystallized with TBA+ only, consistent with results of statistical simulations of random Al distributions in MFI and CHA frameworks that indicate Al proximity increases on average with increasing bulk Al content. 88,89 The finite fraction of proximal Al present in MEL(X,0) materials suggests that TBA+ molecules located in adjacent intersections within MEL crystallites are able to effectively charge-balance Al-Al site pairs during synthesis. Notably, these findings are reminiscent of the finite fractions of paired Al present in MFI crystallized in the presence of TPA+ alone. TPA+ occludes within the channel intersections of the MFI topology, analogous to TBA+ in the MEL topology. DFT-calculated energies for 1773 different arrangements of two Al in MFI charge-compensated by two TPA+ revealed energetically favorable arrangements of two Al separated by ~5 Å while charge compensated by two TPA+ in adjacent channel

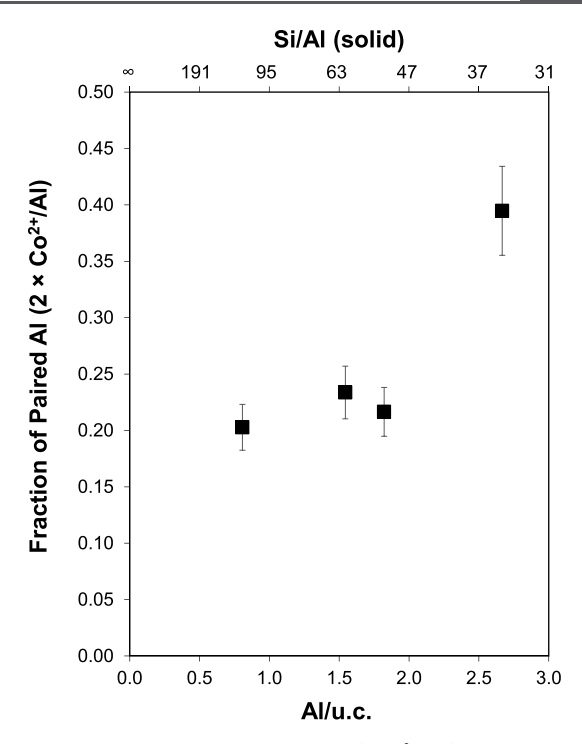


Figure 9. Fraction of paired Al sites $(2Co^{2+}/Al)$ for samples of different Al contents synthesized with TBA⁺ only. Co titration conditions were 0.25 M Co(NO₃)₂, 24 h, 333 K. The fraction of proximal Al $(2\times Co^{2+}/Al)$ was estimated using the NH₃ temperature-programmed saturation and desorption procedures described in Section S6 (Supporting Information). Error bars reflect an absolute error.

intersections.⁵ We conclude that energetically favorable arrangements of Al—Al site pairs charge-compensated by two TBA⁺ molecules located in the adjacent channel intersections are possible within the MEL topology.

Fractions of paired Al for MEL samples crystallized in the presence of TBA+ and Na+ are shown in Figure 10 and reported in Table 1. Samples with similar H⁺/u.c. (1.5-2.1) rather than similar Si/Al were chosen for this comparison because of the high fractions of extra-framework Al present in MEL samples crystallized with TBA+ alone. Fractions of proximal Al were approximately constant for samples with lower occluded Na⁺ content [<1.2 per u.c., $(Na^+/TBA^+)_{gel} \le$ 0.3] but were consistently lower for samples with higher occluded Na⁺ content [\geq 1.6 per u.c., (Na⁺/TBA⁺)_{gel} \leq 0.3] (Figure 10a). A discontinuity in the number of proximal Al formed corresponds to a discontinuity in a larger number (5) of occluded SDAs per unit cell (Figure 10b). Since other properties of the synthesis gel and sample that might influence paired Al content were fixed for the samples compared in Figure 10a, we infer that this decrease in the paired Al content is a direct consequence of the SDAs included in the synthesis gel. The formation of paired Al in MEL samples crystallized with TBA+ alone suggests that two TBA+ molecules sited in adjacent intersections can charge-compensate Co²⁺-titratable Al-Al site pairs. The invariance of such Al-Al site pairs in samples crystallized with low Na⁺/TBA⁺ ratios (<0.3) suggests that the Na⁺ occluded in these samples does not interfere with the ability of the co-occluded TBA+ molecules to influence the formation of Al-Al pairs, which seems consistent with the observation that these samples contain <5 SDAs occluded per unit cell and occluded Na⁺ contents that do not significantly

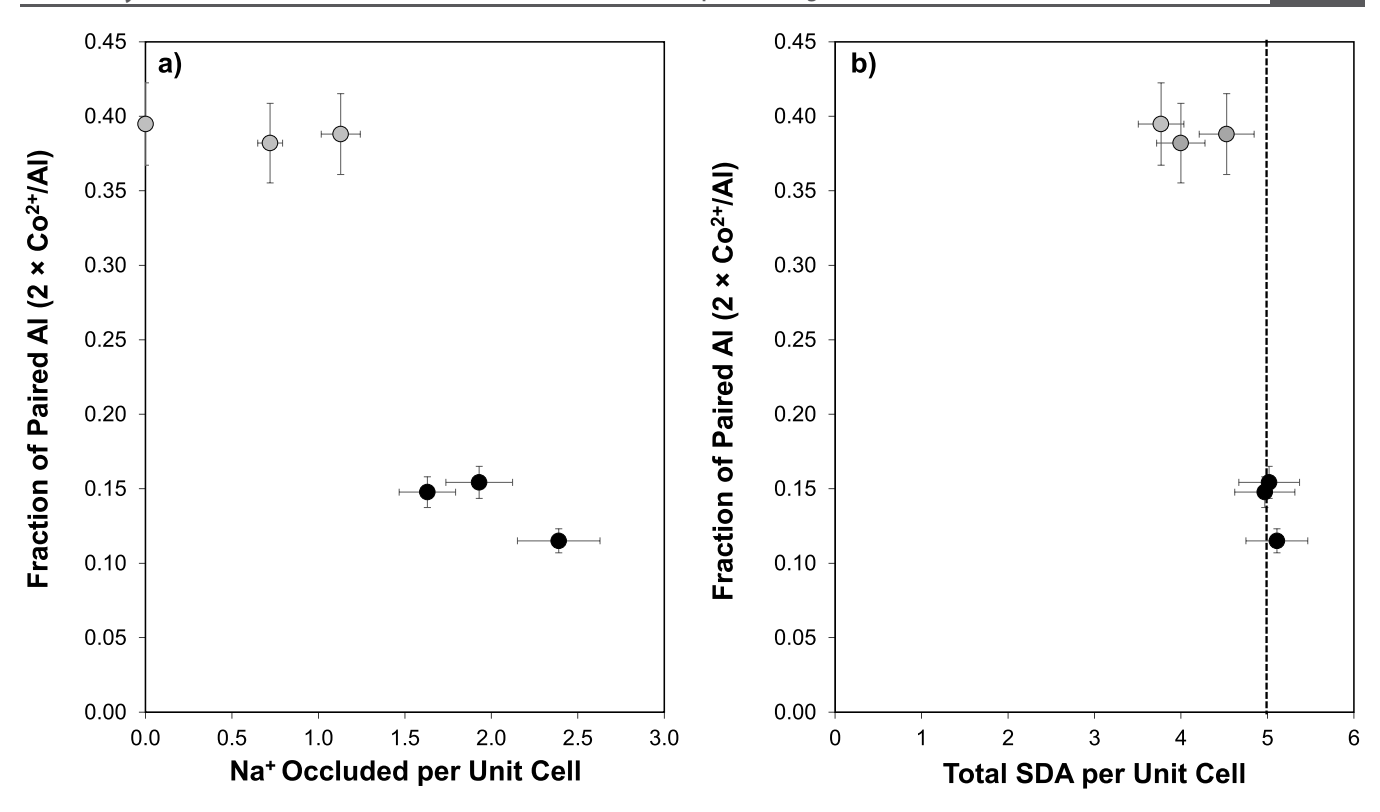


Figure 10. Fraction of paired Al $(2Co^{2+}/Al)$ in MEL zeolites $(H^+/u.c. \sim 1.8)$ containing <5 SDAs per unit cell (gray O) and \sim 5 SDAs per unit cell (\bullet) plotted against (a) occluded Na contents and (b) total occluded SDA (Na⁺ + TBA⁺) contents. The dashed line indicates five SDAs per unit cell Error bars reflect an absolute error.

influence the quantity of occluded TBA⁺ (Figure 8). In contrast, the fraction of paired Al was significantly lower for samples containing greater amounts of occluded Na⁺ (\geq 1.6 per unit cell) and a total of five SDAs occluded per unit cell (Figure 8). The fraction of paired Al generally decreased with increasing Na⁺ contents for these samples; however, a stronger correlation between the fractions of paired Al and occluded Na⁺ content could not be established because crystallizing MEL samples with Na⁺/TBA⁺ gel ratios >1.5 led to the concurrent formation of significant MFI impurities (Section 3.1; Section S3, Supporting Information).

The sharp decrease in the paired Al content for MEL samples crystallized with gel compositions that result in the occlusion of ~5 SDAs per unit cell indicates that these samples have structural properties at the atomic scale that are distinct from MEL samples crystallized by processes that occlude smaller amounts of SDA cations. Differences in the paired Al content between samples crystallized with higher Na⁺/TBA⁺ synthesis gel ratios might also arise from differences in the kinetics of MEL crystallization in the presence of Na⁺. Previous studies of MFI crystallized from amorphous precursors in the presence of TPA+ and through interzeolite conversion in the presence of Na⁺ and TPA⁺ have reported fractions of paired Al that decrease with time (2-288 h), suggesting that framework Al can rearrange during hydrothermal synthesis to achieve more thermodynamically favorable arrangements. 90 If Na+ influences the kinetics of MEL crystallization, differences in paired Al between MEL samples crystallized with different Na⁺/TBA⁺ synthesis gel ratios might reflect differences in approaching thermodynamically favored Al arrangements, given that fractions of paired Al were compared at fixed synthesis time in this study. Notably, differences in extraframework Al, crystallite size, and morphology are observed for samples crystallized with and without Na⁺ in the synthesis gel, suggesting that Na⁺ does influence the crystallization pathway of MEL (additional discussion is given in Section 3.2). However, such differences cannot fully rationalize the observed variation in fractions of paired Al with occluded Na⁺ content because these fractions are invariant for samples of lower Na⁺/ TBA⁺ synthesis gel concentrations (0.0–0.3). Moreover, the fraction of extra-framework Al immediately changes upon incorporating Na⁺ into MEL synthesis gels (~0.0 for Na⁺/ TBA⁺ \geq 0.1), suggesting that while Na⁺ may influence the crystallization pathway, this alone cannot rationalize differences in paired Al observed only among samples of higher occluded Na⁺ contents [\geq 1.6 per u.c.;, (Na⁺/TBA⁺)_{gel} \leq 0.3].

Alternatively, differences in the paired Al content for MEL samples crystallized with different Na⁺/TBA⁺ synthesis gel ratios may reflect the energetic preferences of different combinations of occluded SDAs to charge-compensate different arrangements of Al. Specifically, Na+ competitively replaces TBA+ in MEL samples containing five SDAs occluded per unit cell; in contrast, Na+ is more effective at co-occluding with TBA+ in MEL samples containing <5 SDAs per unit cell, as demonstrated by the increasing total SDA content of these samples. Taken together, these observations suggest that the occlusion of Na⁺ in channel intersections disrupts the formation of Al-Al site pairs that would otherwise be formed by TBA+ molecules in adjacent channel intersections, and that arrangements of Na+ and TBA+ (or Na+ and Na+) in adjacent intersections of MEL are less likely to form Co²⁺-titratable Al-Al site pairs.

The observation that fractions of proximal Al sites in MEL decrease for samples with higher quantities of occluded Na⁺

stands in apparent contrast to prior reports that such fractions increase with the amount of co-occluded Na^+ for CHA (synthesized with TMAda $^+$) 4,42 and MFI (synthesized with TPA $^+$). The amount of occluded OSDA (TMAda $^+$ or TPA $^+$) reported in previous work 4,5 for CHA and MFI samples crystallized with different amounts of occluded inorganic SDA (ISDA) (Na^+ , K^+) is shown in Figure 11 and compared with

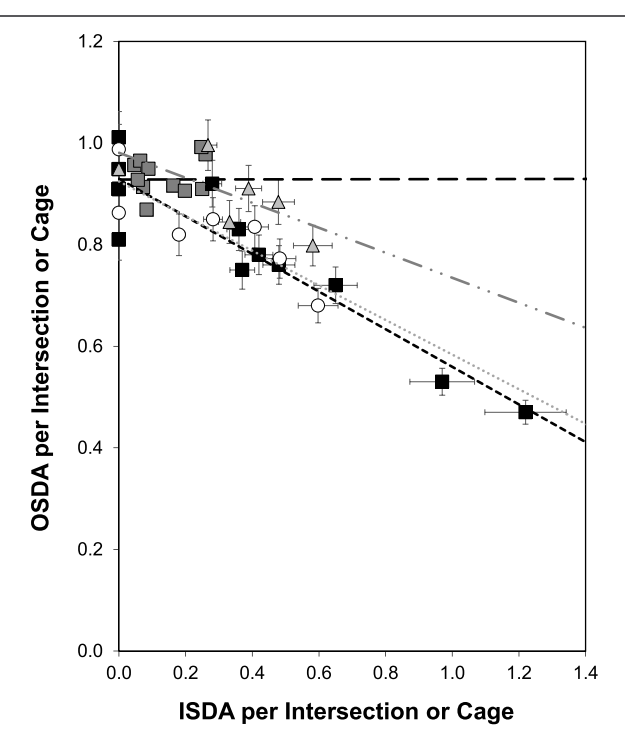


Figure 11. TMAda⁺ per cage occluded in CHA crystallized with varying Na⁺/TMAda⁺ ratios (gray ■) and varying K⁺/TMAda⁺ ratios (■) (published in a study by Di Iorio et al.⁴⁴²), TPA⁺ occluded per channel intersection in MFI crystallized with varying Na⁺/TPA⁺ ratios (gray ▲) (published in a study by Nimlos et al.⁵), and TBA⁺ occluded per channel intersection of MEL crystallized with Na⁺ (○) measured in this work. Dashed lines represent linear regressions to the data: (− −) for CHA crystallized with Na⁺ (---) for CHA crystallized with K⁺, (gray ----) for MFI, and (gray ---) for MEL. Error bars reflect an absolute error.

the amount of TBA+ occluded in MEL samples crystallized in this work with increasing amounts of occluded Na⁺. Na⁺ cooperatively occludes with TMAda+ in CHA, leading to an increase in the total SDA content of per CHA cage (i.e., up to 1.5 SDAs per CHA cage). Moreover, DFT-calculated energies for arrangements of two Al charge-compensated by Na⁺ and TMAda⁺ in CHA revealed an energetic preference (10-30 kJ mol⁻¹) for Na⁺ and TMAda⁺ to site two Al in the 6-MR, while such Al-Al arrangements could not be charge-compensated by two TMAda+ in adjacent CHA cages. Thus, the quantity of Al-Al site pairs in CHA increases with increasing Na⁺ incorporation because of both the co-occlusion of Na+ and TMAda⁺, which leads to higher SDA contents per unit cell of CHA, and because co-occluded Na⁺ and TMAda⁺ preferentially site Co²⁺-titratable Al-Al arrangements (i.e., 6-MR Al pairs). In contrast, synthesis of CHA with K⁺ and TMAda⁺ in CHA leads to 6-MR isolated Al sites. Inclusion of K⁺ results in higher quantities of total SDA per cha cage (up to 1.7 SDAs per cha cage); however, K+ has an energetic preference to occlude in the 8-MR window of the cha cage rather than with

TMAda⁺ within a *cha* cage, thereby disfavoring the formation of 6-MR pairs. Thus, the inclusion of K⁺ in CHA synthesis gels leads to the formation of 6-MR isolated Al sites at the fixed Al content (Si/Al = 10-16), ⁴ despite higher total SDA contents per *cha* cage in CHA samples crystallized with K⁺.

The occluded ISDA content influences the formation of proximal Al sites differently for different OSDA-framework combinations, indicating that the effects of including ISDAs on Al arrangement in a given framework cannot be predicted simply from knowledge of how varying the OSDA/ISDA ratio in the synthesis gel influences the total quantity of SDAs that are occluded. Instead, for a given framework, the formation of Al—Al pair site ensembles depends on the propensity of ISDAs and OSDAs to co-occlude and on their locations within specific rings and voids of the framework. This understanding rationalizes the different effects of Na⁺ on the number of Co²⁺titratable Al pairs in MFI crystallized with TPA+ and MEL crystallized with TBA+. At low ISDA/OSDA ratios, Na+ cooccludes with TPA+ in MFI and TBA+ in MEL, leading to a higher total SDA content in both frameworks; however, Na+ gradually begins to replace the OSDA in both frameworks at higher Na+ contents. The competition between Na+ and OSDA is greater for MEL than MFI, as reflected in the higher total SDA contents occluded in MFI (5.5 per u.c.) compared to MEL (5.1 per u.c.) and the more gradual decrease in the OSDA content with increasing occluded Na+ for MFI compared to MEL (linear regressions presented in Figures 4 and 11). Thus, the propensity of the OSDA and Na⁺ to coocclude is higher in MFI compared to MEL. Additionally, the decrease in Co²⁺-titratable Al-Al pairs in MEL with increasing Na+ content suggests that combinations of nearby Na+ and TBA+ (or two Na+) preferentially site Al in isolated arrangements, as compared to configurations stabilized by two TBA+ in adjacent channel intersections; in contrast, the increase in such pairs with increasing Na⁺ in MFI indicates that Na+ and TPA+ (or two Na+) can more favorably chargecompensate Al pairs than two TPA+ in adjacent channel intersections. Thus, we hypothesize that the decreasing fractions of paired Al with increasing occluded Na⁺ content in MEL reflect both the competition between Na⁺ and TBA⁺, which lead to TBA+ displacement from channel intersections, and the siting preferences of Na+, which bias toward isolated Al arrangements in MEL. More broadly, these findings demonstrate the importance of understanding the nature of SDA-SDA interactions and SDA-framework interactions, which govern the occlusion and siting preferences of inorganic SDAs and OSDAs and thus the specific Al arrangements that form in zeolite frameworks.

4. CONCLUSIONS

The fraction of Al–Al site pairs that form in a given zeolite topology is often influenced by the bulk Al density (Si/Al) but can be varied at fixed Si/Al by incorporating OSDAs and inorganic SDAs of different sizes and charge densities. MEL was successfully synthesized with TBA+ only (Si/Al = 35–118) and with combinations of TBA+ and Na+ at fixed Al contents (Si/Al \sim 50). Approximately four TBA+ molecules were occluded per unit cell in MEL samples crystallized with TBA+ only, indicating TBA+ sites in the channel intersections of MEL (4 per unit cell) analogous to TPA+ in MFI. This limit on TBA+ occlusion results in a lower limit of Si/Al (24) for MEL crystallized with TBA+ only, in agreement with CDM theory. DFT calculations show that TBA+ binds 32 kJ mol $^{-1}$ more

strongly in the larger (A) intersection than the smaller (B) intersection of MEL. Furthermore, DFT indicates that the most stable position of Al in MEL without any charge-balancing SDA is at the T1 position, but that this preference changes to T2 or T4 when the TBA⁺ is present in the A and B intersections, respectively. This preference is driven by the Coulombic interactions between the cationic SDA and the anionic framework Al, in addition to the relative stability of the Al substitution without the OSDA.

Incorporating Na⁺ into MEL synthesis gels resulted in higher total SDA contents (~5 per unit cell), providing access to MEL materials that crystallize with higher densities of occluded cationic charges. The occluded TBA+ content decreased (3.7-2.7 per unit cell) as the occluded Na⁺ content increased, suggesting that Na+ competes with TBA+ for channel intersections in MEL. DFT-calculated binding energies indicate that Na+ does not bind significantly more weakly as its loading increases in both MFI and MEL (regardless of a surrounding H2O solvation shell), although these Na⁺ binding energies are generally weaker in MEL than MFI with 3-4 OSDA per unit cell. As such, the reduced capacity of Na⁺ to co-occlude with TBA⁺ in MEL compared to TPA+ in MFI may be limited by the achievable density of anionic moieties forming in the surrounding frameworkeither substituted Al heteroatoms or silanol defect sites-that balance these cationic charges, rather than repulsion between the OSDA+ and Na+.

Fractions of Co²⁺-titratable Al-Al pairs decreased with increasing amounts of occluded Na+ in MEL zeolites, suggesting that Na+ and TBA+ located in adjacent channel intersections cannot favorably charge-compensate paired Al sites. Thus, occlusion of Na+ in channel intersections dilutes the number of TBA+ molecules in adjacent channel intersections and in turn the number of Al-Al site pairs that otherwise form in the presence of TBA+ only. Decreases in the fraction of paired Al sites in MEL as larger amounts of Na⁺ are occluded are consistent with such decreases observed for CHA crystallized with larger amounts of occluded K+ cations that compete for occlusion with the OSDA. These findings demonstrate that incorporation of a second, more chargedense SDA in a zeolite synthesis gel does not necessarily lead to an increase in proximal Al contents. Rather, the preference to form proximal Al-Al site ensembles depends on the total amounts and specific configurations of occluded SDA molecules within certain rings and voids of the zeolite framework and the energetics of Al siting in various lattice positions when compensated by these SDA configurations. Overall, the synthetic approaches reported herein enable synthesis of MEL zeolites with independently varied Al density and Al proximity, providing a route to study the independent effects of these material properties on catalytic and other functions.

ASSOCIATED CONTENT

Supporting Information

The Supporting Information is available free of charge at https://pubs.acs.org/doi/10.1021/acs.chemmater.2c01083.

XRD patterns, N₂ adsorption isotherms, ²⁷Al MAS NMR, NH₃ TPD profiles, SEM images, TGA profiles, Co²⁺ titration isotherms and discussion of aqueous ion-exchange Co²⁺ titration procedures, and additional DFT calculations (PDF)

AUTHOR INFORMATION

Corresponding Author

Rajamani Gounder — Charles D. Davidson School of Chemical Engineering, Purdue University, West Lafayette, Indiana 47907, United States; oorcid.org/0000-0003-1347-534X; Email: rgounder@purdue.edu

Authors

Elizabeth E. Bickel — Charles D. Davidson School of Chemical Engineering, Purdue University, West Lafayette, Indiana 47907, United States

Alexander J. Hoffman — Department of Chemical Engineering, University of Florida, Gainesville, Florida 32611, United States; orcid.org/0000-0002-1337-9297

Songhyun Lee – Charles D. Davidson School of Chemical Engineering, Purdue University, West Lafayette, Indiana 47907, United States

Hannah E. Snider – Charles D. Davidson School of Chemical Engineering, Purdue University, West Lafayette, Indiana 47907, United States

Claire T. Nimlos – Charles D. Davidson School of Chemical Engineering, Purdue University, West Lafayette, Indiana 47907, United States

Natalie K. Zamiechowski — Charles D. Davidson School of Chemical Engineering, Purdue University, West Lafayette, Indiana 47907, United States

David D. Hibbitts — Department of Chemical Engineering, University of Florida, Gainesville, Florida 32611, United States; occid.org/0000-0001-8606-7000

Complete contact information is available at: https://pubs.acs.org/10.1021/acs.chemmater.2c01083

Author Contributions

The manuscript was written through contributions of all authors, and all authors have given approval to the final version of the manuscript.

Notes

The authors declare no competing financial interest.

ACKNOWLEDGMENTS

We acknowledge financial support provided by the National Science Foundation under Cooperative agreement no. EEC-1647722, which is an Engineering Research Center for the Innovative and Strategic Transformation of Alkane Resources. We thank Rohan Dighe (Purdue University) for providing assistance in catalyst synthesis and characterization. We also thank Dr. John Harwood (Purdue Interdepartmental NMR Facility) for assistance with solid-state NMR. Computational work at the University of Florida was made possible by the Extreme Science and Engineering Discovery Environment, which is supported by the National Science Foundation (grant number ACI-1548562) with allocation CTS160041 and from the University of Florida Research Computing.

REFERENCES

- (1) Nystrom, S.; Hoffman, A.; Hibbitts, D. Tuning Brønsteds Acid Strength by Altering Site Proximity in CHA Framework Zeolites. *ACS Catal.* **2018**, *8*, 7842–7860.
- (2) Kester, P. M.; Crum, J. T.; Li, S.; Schneider, W. F.; Gounder, R. Effects of Brønsted Acid Site Proximity in Chabazite Zeolites on OH Infrared Spectra and Protolytic Propane Cracking Kinetics. *J. Catal.* **2021**, 395, 210–226.

- (3) Hoffman, A. J.; Bates, J. S.; Di Iorio, J. R. D.; Nystrom, S. V.; Nimlos, C. T.; Gounder, R.; Hibbitts, D. Rigid Arrangements of Ionic Charge in Zeolite Frameworks Conferred by Specific Aluminum Distributions Preferentially Stabilize Alkanol Dehydration Transition States. *Angew. Chem., Int. Ed.* **2020**, *59*, 18686–18694.
- (4) Di Iorio, J. R.; Li, S.; Jones, C. B.; Nimlos, C. T.; Wang, Y.; Kunkes, E.; Vattipalli, V.; Prasad, S.; Moini, A.; Schneider, W. F.; Gounder, R. Cooperative and Competitive Occlusion of Organic and Inorganic Structure-Directing Agents within Chabazite Zeolites Influences Their Aluminum Arrangement. J. Am. Chem. Soc. 2020, 142, 4807–4819.
- (5) Nimlos, C. T.; Hoffman, A. J.; Hur, Y. G.; Lee, B. J.; Di Iorio, J. R.; Hibbitts, D. D.; Gounder, R. Experimental and Theoretical Assessments of Aluminum Proximity in MFI Zeolites and Its Alteration by Organic and Inorganic Structure-Directing Agents. *Chem. Mater.* **2020**, *32*, 9277–9298.
- (6) Di Iorio, J. R.; Nimlos, C. T.; Gounder, R. Introducing Catalytic Diversity into Single-Site Chabazite Zeolites of Fixed Composition via Synthetic Control of Active Site Proximity. *ACS Catal.* **2017**, *7*, 6663–6674.
- (7) Janda, A.; Bell, A. T. Effects of Si/Al Ratio on the Distribution of Framework Al and on the Rates of Alkane Monomolecular Cracking and Dehydrogenation in H-MFI. *J. Am. Chem. Soc.* **2013**, *135*, 19193–19207.
- (8) Song, C.; Chu, Y.; Wang, M.; Shi, H.; Zhao, L.; Guo, X.; Yang, W.; Shen, J.; Xue, N.; Peng, L.; Ding, W. Cooperativity of Adjacent Brønsted Acid Sites in MFI Zeolite Channel Leads to Enhanced Polarization and Cracking of Alkanes. *J. Catal.* **2017**, 349, 163–174.
- (9) Bernauer, M.; Tabor, E.; Pashkova, V.; Kaucký, D.; Sobalík, Z.; Wichterlová, B.; Dedecek, J. Proton Proximity New Key Parameter Controlling Adsorption, Desorption and Activity in Propene Oligomerization over H-ZSM-5 Zeolites. *J. Catal.* **2016**, 344, 157–172.
- (10) Tabor, E.; Bernauer, M.; Wichterlová, B.; Dedecek, J. Enhancement of Propene Oligomerization and Aromatization by Proximate Protons in Zeolites; FTIR Study of the Reaction Pathway in ZSM-5. *Catal. Sci. Technol.* **2019**, *9*, 4262–4275.
- (11) Wang, M.; Xia, Y.; Zhao, L.; Song, C.; Peng, L.; Guo, X.; Xue, N.; Ding, W. Remarkable Acceleration of the Fructose Dehydration over the Adjacent Brønsted Acid Sites Contained in an MFI-Type Zeolite Channel. *J. Catal.* **2014**, *319*, 150–154.
- (12) Yang, C.-T.; Janda, A.; Bell, A. T.; Lin, L.-C. Atomistic Investigations of the Effects of Si/Al Ratio and Al Distribution on the Adsorption Selectivity of n-Alkanes in Brønsted-Acid Zeolites. *J. Phys. Chem. C* 2018, 122, 9397–9410.
- (13) Findley, J. M.; Ravikovitch, P. I.; Sholl, D. S. The Effect of Aluminum Short-Range Ordering on Carbon Dioxide Adsorption in Zeolites. *J. Phys. Chem. C* **2018**, *122*, 12332–12340.
- (14) Wulfers, M. J.; Teketel, S.; Ipek, B.; Lobo, R. F. Conversion of Methane to Methanol on Copper-Containing Small-Pore Zeolites and Zeotypes. *Chem. Commun.* **2015**, *51*, 4447–4450.
- (15) Smeets, P. J.; Groothaert, M. H.; Schoonheydt, R. A. Cu Based Zeolites: A UV-Vis Study of the Active Site in the Selective Methane Oxidation at Low Temperatures. *Catal. Today* **2005**, *110*, 303–309.
- (16) Devos, J.; Bols, M. L.; Plessers, D.; Goethem, C.; Seo, J. W.; Hwang, S.-J.; Sels, B. F.; Dusselier, M. Synthesis-Structure-Activity Relations in Fe-CHA for C-H Activation: Control of Al Distribution by Interzeolite Conversion. *Chem. Mater.* **2019**, 32, 273.
- (17) Li, S.; Wang, Y.; Wu, T.; Schneider, W. F. First-Principles Analysis of Site- and Condition-Dependent Fe Speciation in SSZ-13 and Implications for Catalyst Optimization. *ACS Catal.* **2018**, 8, 10119–10130.
- (18) Gao, J.; Zheng, Y.; Jehng, J.-M.; Tang, Y.; Wachs, I. E.; Podkolzin, S. G. Identification of Molybdenum Oxide Nanostructures on Zeolites for Natural Gas Conversion. *Science* **2015**, 348, 686–690. (19) Gao, J.; Zheng, Y.; Fitzgerald, G. B.; de Joannis, J.; Tang, Y.; Wachs, I. E.; Podkolzin, S. G. Structure of Mo_2C_x and Mo_4C_x Molybdenum Carbide Nanoparticles and Their Anchoring Sites on ZSM-5 Zeolites. *J. Phys. Chem. C* **2014**, 118, 4670–4679.

- (20) Razdan, N. K.; Bhan, A. Carbidic Mo Is the Sole Kinetically-Relevant Active Site for Catalytic Methane Dehydroaromatization on Mo/H-ZSM-5. *J. Catal.* **2020**, 389, 667–676.
- (21) Phadke, N. M.; Van der Mynsbrugge, J.; Mansoor, E.; Getsoian, A. B.; Head-Gordon, M.; Bell, A. T. Characterization of Isolated Ga³⁺ Cations in Ga/H-MFI Prepared by Vapor-Phase Exchange of H-MFI Zeolite with GaCl₃. ACS Catal. 2018, 8, 6106–6126.
- (22) Phadke, N. M.; Mansoor, E.; Bondil, M.; Head-Gordon, M.; Bell, A. T. Mechanism and Kinetics of Propane Dehydrogenation and Cracking over Ga/H-MFI Prepared via Vapor-Phase Exchange of H-MFI with GaCl₃. J. Am. Chem. Soc. **2019**, 141, 1614–1627.
- (23) Schreiber, M. W.; Plaisance, C. P.; Baumgärtl, M.; Reuter, K.; Jentys, A.; Bermejo-Deval, R.; Lercher, J. A. Lewis-Brønsted Acid Pairs in Ga/H-ZSM-5 To Catalyze Dehydrogenation of Light Alkanes. *J. Am. Chem. Soc.* **2018**, *140*, 4849–4859.
- (24) Groothaert, M. H.; Lievens, K.; van Bokhoven, J. A.; Battiston, A. A.; Weckhuysen, B. M.; Pierloot, K.; Schoonheydt, R. A. Bis(μ-OXO)Dicopper as Intermediate in the Catalytic Decomposition of NO over Cu-ZSM-5. In *Studies in Surface Science and Catalysis*; van Steen, E., Claeys, M., Callanan, L. H., Eds.; *Recent Advances in the Science and Technology of Zeolites and Related Materials*; Elsevier, 2004; Vol. 154, pp 2449–2457.
- (25) Giordanino, F.; Vennestrøm, P. N. R.; Lundegaard, L. F.; Stappen, F. N.; Mossin, S.; Beato, P.; Bordiga, S.; Lamberti, C. Characterization of Cu-Exchanged SSZ-13: A Comparative FTIR, UV-Vis, and EPR Study with Cu-ZSM-5 and Cu- β with Similar Si/Al and Cu/Al Ratios. *Dalton Trans.* **2013**, 42, 12741–12761.
- (26) Paolucci, C.; Parekh, A. A.; Khurana, I.; Di Iorio, J. R.; Li, H.; Albarracin Caballero, J. D.; Shih, A. J.; Anggara, T.; Delgass, W. N.; Miller, J. T.; Ribeiro, F. H.; Gounder, R.; Schneider, W. F. Catalysis in a Cage: Condition-Dependent Speciation and Dynamics of Exchanged Cu Cations in SSZ-13 Zeolites. *J. Am. Chem. Soc.* **2016**, 138, 6028–6048.
- (27) Sazama, P.; Wichterlová, B.; Tábor, E.; Šťastný, P.; Sathu, N. K.; Sobalík, Z.; Dědeček, J.; Sklenák, Š.; Klein, P.; Vondrová, A. Tailoring of the Structure of Fe-Cationic Species in Fe-ZSM-5 by Distribution of Al Atoms in the Framework for N₂O Decomposition and NH₃-SCR-NO_x. J. Catal. **2014**, 312, 123–138.
- (28) Hansen, N.; Heyden, A.; Bell, A. T.; Keil, F. J. A Reaction Mechanism for the Nitrous Oxide Decomposition on Binuclear Oxygen Bridged Iron Sites in Fe-ZSM-5. *J. Phys. Chem. C* **2007**, *111*, 2092–2101.
- (29) Sklenak, S.; Andrikopoulos, P. C.; Boekfa, B.; Jansang, B.; Nováková, J.; Benco, L.; Bucko, T.; Hafner, J.; Dědeček, J.; Sobalík, Z. N_2O Decomposition over Fe-Zeolites: Structure of the Active Sites and the Origin of the Distinct Reactivity of Fe-Ferrierite, Fe-ZSM-5, and Fe-Beta. A Combined Periodic DFT and Multispectral Study. *J. Catal.* **2010**, 272, 262–274.
- (30) Sobalik, Z.; Sazama, P.; Dedecek, J.; Wichterlová, B. Critical Evaluation of the Role of the Distribution of Al Atoms in the Framework for the Activity of Metallo-Zeolites in Redox N_2O/NO_x Reactions. *Appl. Catal., A* **2014**, 474, 178–185.
- (31) Lardinois, T. M.; Bates, J. S.; Lippie, H. H.; Russell, C. K.; Miller, J. T.; Meyer, H. M.; Unocic, K. A.; Prikhodko, V.; Wei, X.; Lambert, C. K.; Getsoian, A. B.; Gounder, R. Structural Interconversion between Agglomerated Palladium Domains and Mononuclear Pd(II) Cations in Chabazite Zeolites. *Chem. Mater.* **2021**, 33, 1698–1713.
- (32) Knott, B. C.; Nimlos, C. T.; Robichaud, D. J.; Nimlos, M. R.; Kim, S.; Gounder, R. Consideration of the Aluminum Distribution in Zeolites in Theoretical and Experimental Catalysis Research. *ACS Catal.* **2018**, *8*, 770–784.
- (33) Bickel, E. E.; Nimlos, C. T.; Gounder, R. Developing Quantitative Synthesis-Structure-Function Relations for Framework Aluminum Arrangement Effects in Zeolite Acid Catalysis. *J. Catal.* **2021**, 399, 75–85.
- (34) Dědeček, J.; Tabor, E.; Sklenak, S. Tuning the Aluminum Distribution in Zeolites to Increase Their Performance in Acid-Catalyzed Reactions. *ChemSusChem* **2019**, *12*, 556–576.

- (35) Dusselier, M.; Davis, M. E. Small-Pore Zeolites: Synthesis and Catalysis. *Chem. Rev.* **2018**, *118*, 5265–5329.
- (36) Le, T. T.; Chawla, A.; Rimer, J. D. Impact of Acid Site Speciation and Spatial Gradients on Zeolite Catalysis. *J. Catal.* **2020**, 391, 56–68.
- (37) Park, M. B.; Jo, D.; Jeon, H. C.; Nicholas, C. P.; Lewis, G. J.; Hong, S. B. Zeolite Synthesis from a Charge Density Perspective: The Charge Density Mismatch Synthesis of UZM-5 and UZM-9. *Chem. Mater.* **2014**, *26*, 6684–6694.
- (38) Lewis, G. J.; Miller, M. A.; Moscoso, J. G.; Wilson, B. A.; Knight, L. M.; Wilson, S. T. Experimental Charge Density Matching Approach to Zeolite Synthesis. In *Studies in Surface Science and Catalysis*; van Steen, E., Claeys, I. M., Callanan, L. H., Eds.; Recent Advances in the Science and Technology of Zeolites and Related Materials; Elsevier, 2004; Vol. 154, pp 364–372.
- (39) Liang, Y.; Jacobson, A. J.; Rimer, J. D. Strontium Ions Function as Both an Accelerant and Structure-Directing Agent of Chabazite Crystallization. *ACS Mater. Lett.* **2020**, *3*, 187–192.
- (40) Lv, W.; Wang, S.; Wang, P.; Liu, Y.; Huang, Z.; Li, J.; Dong, M.; Wang, J.; Fan, W. Regulation of Al Distributions and $\mathrm{Cu^{2+}}$ Locations in SSZ-13 Zeolites for NH₃-SCR of NO by Different Alkali Metal Cations. *J. Catal.* **2021**, 393, 190–201.
- (41) Hur, Y. G.; Kester, P. M.; Nimlos, C. T.; Cho, Y.; Miller, J. T.; Gounder, R. Influence of Tetrapropylammonium and Ethylenediamine Structure-Directing Agents on the Framework Al Distribution in B-Al-MFI Zeolites. *Ind. Eng. Chem. Res.* **2019**, 58, 11849–11860.
- (42) Di Iorio, J. R.; Gounder, R. Controlling the Isolation and Pairing of Aluminum in Chabazite Zeolites Using Mixtures of Organic and Inorganic Structure-Directing Agents. *Chem. Mater.* **2016**, 28, 2236–2247.
- (43) Schwalbe-Koda, D.; Kwon, S.; Paris, C.; Bello-Jurado, E.; Jensen, Z.; Olivetti, E.; Willhammar, T.; Corma, A.; Román-Leshkov, Y.; Moliner, M.; Gómez-Bombarelli, R. A Priori Control of Zeolite Phase Competition and Intergrowth with High-Throughput Simulations. *Science* **2021**, *374*, No. eabh3350.
- (44) Jing, B.; Li, J.; Li, Z.; Wang, S.; Qin, Z.; Fan, W.; Wang, J. Comparative Study of Methanol to Olefins Over ZSM-5, ZSM-11, ZSM-22 and EU-1: Dependence of Catalytic Performance on the Zeolite Framework Structure. *J. Nanosci. Nanotechnol.* **2017**, *17*, 3680–3688.
- (45) Bleken, F.; Skistad, W.; Barbera, K.; Kustova, M.; Bordiga, S.; Beato, P.; Lillerud, K.; Svelle, S.; Olsbye, U. Conversion of Methanol over 10-Ring Zeolites with Differing Volumes at Channel Intersections: Comparison of TNU-9, IM-5, ZSM-11 and ZSM-5. *Phys. Chem. Chem. Phys.* **2011**, *13*, 2539–2549.
- (46) Zhang, L.; Liu, H.; Li, X.; Xie, S.; Wang, Y.; Xin, W.; Liu, S.; Xu, L. Differences between ZSM-5 and ZSM-11 Zeolite Catalysts in 1-Hexene Aromatization and Isomerization. *Fuel Process. Technol.* **2010**, *91*, 449–455.
- (47) Schwalbe-Koda, D. Organic Structure Directing agent Data-Base. OSDB. https://zeodb.mit.edu/index (accessed Feb 2, 2022).
- (48) Sharma, P.; Chung, W.-J. Synthesis of MEL Type Zeolite with Different Kinds of Morphology for the Recovery of 1-Butanol from Aqueous Solution. *Desalination* **2011**, 275, 172–180.
- (49) Terasaki, O.; Ohsuna, T.; Sakuma, H.; Watanabe, D.; Nakagawa, Y.; Medrud, R. C. Direct Observation of "Pure MEL Type" Zeolite. *Chem. Mater.* **1996**, *8*, 463–468.
- (50) Shen, Y.; Le, T. T.; Fu, D.; Schmidt, J. E.; Filez, M.; Weckhuysen, B. M.; Rimer, J. D. Deconvoluting the Competing Effects of Zeolite Framework Topology and Diffusion Path Length on Methanol to Hydrocarbons Reaction. *ACS Catal.* **2018**, *8*, 11042–11053.
- (51) Derewinski, M.; Machowska, M. Effect of Stirring on the Selective Synthesis of MEL or TON Zeolites in the Presence of 1,8-Diaminooctane. In *Studies in Surface Science and Catalysis*; van Steen, E., Claeys, I. M., Callanan, L. H., Eds.; Recent Advances in the Science and Technology of Zeolites and Related Materials; Elsevier, 2004; Vol. 154, pp 349–354.

- (52) Wang, S.; Zhang, L.; Li, S.; Qin, Z.; Shi, D.; He, S.; Yuan, K.; Wang, P.; Zhao, T.-S.; Fan, S.; Dong, M.; Li, J.; Fan, W.; Wang, J. Tuning the Siting of Aluminum in ZSM-11 Zeolite and Regulating Its Catalytic Performance in the Conversion of Methanol to Olefins. *J. Catal.* **2019**, 377, 81–97.
- (53) Wang, S.; Wang, P.; Qin, Z.; Chen, Y.; Dong, M.; Li, J.; Zhang, K.; Liu, P.; Wang, J.; Fan, W. Relation of Catalytic Performance to the Aluminum Siting of Acidic Zeolites in the Conversion of Methanol to Olefins, Viewed via a Comparison between ZSM-5 and ZSM-11. ACS Catal. 2018, 8, 5485–5505.
- (54) Wang, X.; Meng, F.; Chen, H.; Gao, F.; Wang, Y.; Han, X.; Fan, C.; Sun, C.; Wang, S.; Wang, L. Synthesis of a Hierarchical ZSM-11/5 Composite Zeolite of High SiO₂/Al₂O₃ Ratio and Catalytic Performance in the Methanol-to-Olefins Reaction. *C. R. Chim.* **2017**, *20*, 1083–1092.
- (55) Kokotailo, G. T.; Chu, P.; Lawton, S. L.; Meier, W. M. Synthesis and Structure of Synthetic Zeolite ZSM-11. *Nature* **1978**, 275, 119–120.
- (56) Di Iorio, J. R.; Bates, S. A.; Verma, A. A.; Delgass, W. N.; Ribeiro, F. H.; Miller, J. T.; Gounder, R. The Dynamic Nature of Brønsted Acid Sites in Cu–Zeolites During NO_x Selective Catalytic Reduction: Quantification by Gas-Phase Ammonia Titration. *Top. Catal.* **2015**, *58*, 424–434.
- (57) Kresse, G. Ab Initio Molecular Dynamics for Liquid Metals. J. Non-Cryst. Solids 1995, 192-193, 222-229.
- (58) Kresse, G.; Furthmüller, J. Efficiency of Ab-Initio Total Energy Calculations for Metals and Semiconductors Using a Plane-Wave Basis Set. *Comput. Mater. Sci.* **1996**, *6*, 15–50.
- (59) Kresse, G.; Hafner, J. Norm-Conserving and Ultrasoft Pseudopotentials for First-Row and Transition Elements. *J. Phys.: Condens. Matter* **1994**, *6*, 8245–8257.
- (60) Kresse, G.; Furthmüller, J. Efficient Iterative Schemes for Ab Initio Total-Energy Calculations Using a Plane-Wave Basis Set. *Phys. Rev. B: Condens. Matter Mater. Phys.* **1996**, *54*, 11169–11186.
- (61) Kravchenko, P.; Plaisance, C.; Hibbitts, D. A New Computational Interface for Catalysis. 2019, ChemRxiv, Theoretical and Computational Chemistry, https://doi.org/10.26434/chemrxiv. 8040737.v4 (accessed May 1, 2022).
- (62) Blöchl, P. E. Projector Augmented-Wave Method. Phys. Rev. B: Condens. Matter Mater. Phys. 1994, 50, 17953-17979.
- (63) Kresse, G.; Joubert, D. From Ultrasoft Pseudopotentials to the Projector Augmented-Wave Method. *Phys. Rev. B: Condens. Matter Mater. Phys.* **1999**, *59*, 1758–1775.
- (64) Perdew, J. P.; Burke, K.; Ernzerhof, M. Generalized Gradient Approximation Made Simple. *Phys. Rev. Lett.* **1996**, 77, 3865–3868.
- (65) Grimme, S.; Antony, J.; Ehrlich, S.; Krieg, H. A Consistent and Accurate Ab Initio Parametrization of Density Functional Dispersion Correction (DFT-D) for the 94 Elements H-Pu. *J. Chem. Phys.* **2010**, 132, 154104.
- (66) Grimme, S.; Ehrlich, S.; Goerigk, L. Effect of the Damping Function in Dispersion Corrected Density Functional Theory. *J. Comput. Chem.* **2011**, 32, 1456–1465.
- (67) van Koningsveld, H. High-Temperature (350 K) Orthorhombic Framework Structure of Zeolite H-ZSM-5. *Acta Crystallogr., Sect. B: Struct. Sci.* **1990**, 46, 731–735.
- (68) Hoffman, A.; DeLuca, M.; Hibbitts, D. Restructuring of MFI Framework Zeolite Models and Their Associated Artifacts in Density Functional Theory Calculations. *J. Phys. Chem. C* **2019**, 123, 6572–6585
- (69) Baerlocher, C.; McCusker, L. B. Database of Zeolite Structures. http://www.iza-structure.org/databases/ (accessed Feb 14, 2021).
- (70) Ban, S.; Vlugt, T. J. H. Zeolite Microporosity Studied by Molecular Simulation. *Mol. Simul.* **2009**, *35*, 1105–1115.
- (71) Graaf, B. V. D.; Njo, S. L.; Smirnov, K. S. Introduction to Zeolite Modeling. In *Reviews in Computational Chemistry*; John Wiley & Sons, Ltd., 2000; pp 137–223.
- (72) Schwalbe-Koda, D.; Gómez-Bombarelli, R. Benchmarking Binding Energy Calculations for Organic Structure-Directing Agents in Pure-Silica Zeolites. *J. Chem. Phys.* **2021**, *154*, 174109.

- (73) Derouane, E. G.; Dejaifve, P.; Gabelica, Z.; Védrine, J. C. Molecular Shape Selectivity of ZSM-5, Modified ZSM-5 and ZSM-11 Type Zeolites. *Faraday Discuss. Chem. Soc.* **1981**, 72, 331–344.
- (74) de Vos Burchart, E.; van Koningsveld, H.; van de Graaf, B. Molecular Mechanics Studies of TBA and TPA in MEL and MFI. *Microporous Mater.* **1997**, *8*, 215–222.
- (75) Shen, Y.; Le, T. T.; Li, R.; Rimer, J. D. Optimized Synthesis of ZSM-11 Catalysts using 1,8-Diaminooctane as a Structure-Directing Agent. *ChemPhysChem* **2018**, *19*, 529–537.
- (76) Bellussi, G.; Perego, G.; Carati, A.; Cornaro, U.; Fattore, V. 5-1 SBU Based Zeolites from Wholly Inorganic Systems. In *Studies in Surface Science and Catalysis*; Grobet, P. J., Mortier, W. J., Vansant, E. F., Schulz-Ekloff, G., Eds.; *Innovation in Zeolite Materials Science*; Elsevier, 1988; Vol. 37, pp 37–44.
- (77) Yokoi, T.; Mochizuki, H.; Namba, S.; Kondo, J. N.; Tatsumi, T. Control of the Al Distribution in the Framework of ZSM-5 Zeolite and Its Evaluation by Solid-State NMR Technique and Catalytic Properties. J. Phys. Chem. C 2015, 119, 15303–15315.
- (78) Kumar, S.; Sinha, A. K.; Hegde, S. G.; Sivasanker, S. Influence of Mild Dealumination on Physicochemical, Acidic and Catalytic Properties of H-ZSM-5. *J. Mol. Catal. A: Chem.* **2000**, *154*, 115–120.
- (79) Choudhary, M. K.; Kumar, M.; Rimer, J. D. Regulating Nonclassical Pathways of Silicalite-1 Crystallization through Controlled Evolution of Amorphous Precursors. *Angew. Chem., Int. Ed.* **2019**, *58*, 15712–15716.
- (80) Lewis, D. W.; Freeman, C. M.; Catlow, C. R. A. Predicting the Templating Ability of Organic Additives for the Synthesis of Microporous Materials. *J. Phys. Chem.* **1995**, *99*, 11194–11202.
- (81) Wagner, P.; Nakagawa, Y.; Lee, G. S.; Davis, M. E.; Elomari, S.; Medrud, R. C.; Zones, S. I. Guest/Host Relationships in the Synthesis of the Novel Cage-Based Zeolites SSZ-35, SSZ-36, and SSZ-39. *J. Am. Chem. Soc.* **2000**, 122, 263–273.
- (82) Pophale, R.; Daeyaert, F.; Deem, M. W. Computational Prediction of Chemically Synthesizable Organic Structure Directing Agents for Zeolites. *J. Mater. Chem. A* **2013**, *1*, 6750–6760.
- (83) Daeyaert, F.; Deem, M. W. Cover Feature: Design of Organic Structure-Directing Agents for the Controlled Synthesis of Zeolites for Use in Carbon Dioxide/Methane Membrane Separations (ChemPlusChem 2/2020). ChemPlusChem 2020, 85, 265.
- (84) Schmidt, J. E.; Deem, M. W.; Davis, M. E. Synthesis of a Specified, Silica Molecular Sieve by Using Computationally Predicted Organic Structure-Directing Agents. *Angew. Chem., Int. Ed.* **2014**, *53*, 8372–8374.
- (85) Muraoka, K.; Chaikittisilp, W.; Okubo, T. Multi-Objective de Novo Molecular Design of Organic Structure-Directing Agents for Zeolites Using Nature-Inspired Ant Colony Optimization. *Chem. Sci.* **2020**, *11*, 8214–8223.
- (86) Dědeček, J.; Sklenak, S.; Li, C.; Wichterlová, B.; Gábová, V.; Brus, J.; Sierka, M.; Sauer, J. Effect of Al–Si–Al and Al–Si–Si–Al Pairs in the ZSM-5 Zeolite Framework on the ²⁷Al NMR Spectra. A Combined High-Resolution 27Al NMR and DFT/MM Study. *J. Phys. Chem. C* **2009**, *113*, 1447–1458.
- (87) Rubeš, M.; Koudelková, E.; de Oliveira Ramos, F. S.; Trachta, M.; Bludský, O.; Bulánek, R. Experimental and Theoretical Study of Propene Adsorption on K-FER Zeolites: New Evidence of Bridged Complex Formation. *J. Phys. Chem. C* **2018**, *122*, *6*128–6136.
- (88) Goodman, B. Ř.; Hass, K. C.; Schneider, W. F.; Adams, J. B. Statistical Analysis of Al Distributions and Metal Ion Pairing Probabilities in Zeolites. *Catal. Lett.* **2000**, *68*, 85–93.
- (89) Bates, S. A.; Verma, A. A.; Paolucci, C.; Parekh, A. A.; Anggara, T.; Yezerets, A.; Schneider, W. F.; Miller, J. T.; Delgass, W. N.; Ribeiro, F. H. Identification of the Active Cu Site in Standard Selective Catalytic Reduction with Ammonia on Cu-SSZ-13. *J. Catal.* **2014**, *312*, 87–97.
- (90) Devos, J.; Robijns, S.; Van Goethem, C.; Khalil, I.; Dusselier, M. Interzeolite Conversion and the Role of Aluminum: Toward Generic Principles of Acid Site Genesis and Distributions in ZSM-5 and SSZ-13. *Chem. Mater.* **2021**, *33*, 2516.

☐ Recommended by ACS

Evolution of Framework Al Arrangements in CHA Zeolites during Crystallization in the Presence of Organic and Inorganic Structure-Directing Agents

Songhyun Lee, Rajamani Gounder, et al.

SEPTEMBER 19, 2022

CRYSTAL GROWTH & DESIGN

READ 🗹

Effects of Next-Nearest-Neighbor Aluminum Location on the Brønsted Acidity of HY Zeolites

Wenru Zhao, Donghai Mei, et al.

DECEMBER 06, 2022

THE JOURNAL OF PHYSICAL CHEMISTRY C

READ 🗹

Influence of an *N,N,N*-Trimethyl-1-adamantyl Ammonium (TMAda⁺) Structure Directing Agent on Al Distributions and Pair Features in Chabazite Zeolite

Xiaoyu Wang, William F. Schneider, et al

DECEMBER 07, 2022

CHEMISTRY OF MATERIALS

READ 🗹

¹⁷O Labeling Reveals Paired Active Sites in Zeolite Catalysts

Kuizhi Chen, Jeffery L. White, et al.

AUGUST 31, 2022

JOURNAL OF THE AMERICAN CHEMICAL SOCIETY

READ 🗹

Get More Suggestions >